https://doi.org/10.5194/egusphere-2026-1357
Preprint. Discussion started: 31 March 2026

SeidarT: An open-source full-waveform seismic and electromagnetic wave propagation modeling toolbox demonstrated in snow and ice

Steven Bernsen[1], Christopher Gerbi[1], Senthil Vel[2], Knut Christianson[3], and Seth Campbell[1]

[1]School of Earth and Climate Sciences, University of Maine, 5790 Bryand Global Sciences Center, Orono, Maine 04469
[2]Department of Mechanical Engineering, University of Maine, Ferland Engineering Education and Design Center, Orono, Maine 04469
[3]Earth and Space Sciences, University of Washington, 1707 NE Grant Lane, Seattle, Washington 98195

Correspondence: Steven Bernsen (steven.bernsen@maine.edu)

Abstract. We present *SeidarT*, an open-source, community-driven software package for full-waveform finite-difference time-domain (FDTD) modeling of elastic and electromagnetic wave propagation in heterogeneous, anisotropic, and attenuating media. *SeidarT* natively incorporates full-tensor anisotropy (all 21 stiffness coefficients), frequency-independent attenuation through a generalized Q formulation, and unified treatment of both seismic and electromagnetic wave physics on a simple Cartesian grid. The software prioritizes accessibility and extensibility by combining the computational efficiency of FORTRAN with the user-friendly scripting capabilities of Python. Model construction leverages an intuitive image-based geometry workflow and JSON project files, eliminating the need for complex mesh generation while allowing flexible specification of arbitrary stiffness or permittivity tensors, material distributions, and boundary conditions. We implement the Convolutional Perfectly Matched Layer (CPML) with explicit tuning strategies adapted for anisotropic media, and provide automatic stability checking via the Courant-Friedrichs-Lévy and wavenumber-bandlimit criteria. The software is validated against analytical solutions for elastic wave propagation and empirically constrained through comparison with ground-penetrating radar and seismic field observations in snow and ice. We document the physical property parameterizations for ice and snow as functions of temperature, pressure, and liquid water content, and provide multiple material homogenization schemes (Hill average, Gassmann substitution, Self-Consistent Approximation) to accommodate variable porosity and fluid saturation regimes. *SeidarT* is designed to lower economic and technical barriers for scientists, engineers, and students integrating sophisticated wave-physics simulations into workflows spanning cryospheric research, environmental monitoring, subsurface characterization, and civil infrastructure assessment. The open-source development model on GitHub and PyPI encourages community contributions and iterative improvements, positioning *SeidarT* as a versatile platform for advancing both fundamental understanding and applied geophysical imaging.

https://doi.org/10.5194/egusphere-2026-1357
Preprint. Discussion started: 31 March 2026

1 Introduction

Wave propagation modeling plays a central role across a wide range of disciplines - from exploration seismology (Hu et al., 2023; Lyu et al., 2025) and environmental monitoring (Graves and Day, 2003) to civil infrastructure assessment (Komatitsch and Vilotte, 1998; Ali et al., 2023) and planetary science (Bozdağ et al., 2017) - by providing detailed insights into subsurface and structural properties that are otherwise inaccessible. Whether probing for groundwater reservoirs, characterizing fracture networks in geothermal fields, imaging buried archaeological features, or evaluating the integrity of concrete bridges, elastic and electromagnetic waves offer non-invasive means of imaging and characterizing the subsurface. Numerical experiments are particularly valuable when direct measurements are impractical or hazardous, enabling parameter studies, sensitivity analyses, and synthetic data generation for developing advanced processing workflows, including machine-learning approaches in regions with sparse field observations (e.g., Wu et al. (2019); Wassil et al. (2022)).

Numerical solvers for wave phenomena are ideal in situations where complex mathematics and modeling domains do not allow for analytical solutions, such as when heterogeneity, anisotropy, attenuation, or irregular boundaries make closed-form solutions intractable. Modeling approaches can be categorized using two different approaches: (1) full waveform, which includes Finite Difference Time Domain (FDTD) (Levander, 1988; Virieux, 1984; Komatitsch and Martin, 2007), Finite Element Method (FEM) (Zienkiewicz et al., 1977; Mahmoudian and Margrave, 2003), pseudo-spectral (Klin et al., 2010)], and spectral element methods (Komatitsch and Tromp, 1999), and (2) ray tracing methods (Julian et al., 1977; Um and Thurber, 1987). Although ray tracing methods are computationally less expensive yet effective in modeling travel time of specific modes, full waveform techniques provide the elastodynamic response, capturing the time variability of wave phenomena (Bai et al., 2013).

Implementing full-waveform solvers in heterogeneous, anisotropic media poses significant challenges: meshing complex geometries for spectral or finite-element schemes can become unwieldy, while high-order finite differences must carefully balance accuracy, stability, and computational cost. In snow and ice, for example, preferred crystal-orientation fabrics, varying water content, and thermal gradients introduce full-tensor anisotropy and frequency-dependent attenuation that significantly alter both seismic and electromagnetic responses [Bradford et al. (2009), Bælum and Benn (2011), Riche et al. (2013), Montagnat et al. (2020)]. Similar complexities arise in subsurface petroleum systems (fractured carbonates, shales), geotechnical investigations (i.e. seismic site amplification, reinforced concrete GPR imaging), anthropologic/archeaologic surveys (preferential artifact orientations, heterogenous burial stratigraphy, disturbed sediments) and even biomedical ultrasound (i.e. anisotropic soft tissues), motivating a need for versatile modeling frameworks that can flexibly accommodate a variety of physical parameters and boundary conditions.

In this work, we present *SeidarT*, an open-source, community-driven FDTD code that natively incorporates full-tensor anisotropy, frequency-independent attenuation (via a generalized Q formulation) (Kjartansson, 1979), and both seismic and electromagnetic wave physics within a unified, computationally efficient environment. Its design emphasizes simplicity of implementation—avoiding complex mesh generation—while allowing users to specify arbitrary stiffness or permittivity tensors, material distributions, and boundary conditions by coupling an image-based geometry and JSON project workflow. The software package is validated against analytical solutions and snow/ice-focused field observations, and includes explicit treat-

https://doi.org/10.5194/egusphere-2026-1357
Preprint. Discussion started: 31 March 2026

ment of the Convolutional Perfectly Matched Layer (CPML) tuning and stability in anisotropic media. Although we focus on cryospheric applications, the software is suitable for materials that extend into other regimes of geological and material sciences. As computing power becomes increasingly accessible, *SeidarT* is designed to lower economic and technical barriers by providing a ready-to-use, extensible framework that scientists and engineers can integrate into workflows ranging from cryospheric research and hydrocarbon exploration to civil–environmental engineering.

https://doi.org/10.5194/egusphere-2026-1357
Preprint. Discussion started: 31 March 2026

2 Software Description

2.1 Key Features and Architecture

SeidarT is designed to enhance usability and performance in geophysical modeling, particularly for wave propagation in snow and ice environments. One of its key features is that it is open-source and hosted on GitHub, accompanied by robust documentation to support users in its implementation and development. Model development in *SeidarT* leverages illustration software like Gimp and Inkscape, which are free cross-platform tools capable of generating PDF and PNG files. This approach provides users with significant control over defining complex geometries, such as the varying sloped sidewalls and changes in ice facies found in glaciers. Programmatically defining such intricate geometries can be cumbersome and limiting, whereas using RGB values in illustrations to identify different materials streamlines the process, allowing for more precise and versatile model creation.

The software also supports the calculation of bulk properties from Euler angle inputs for material fabrics. Users can input text files from Electron Backscatter Diffraction (EBSD) directly into the program for material homogenization, employing three Euler angles for Bunge rotation (z-x-z) (Bunge, 2013) and fourth-order tensors. This allows for detailed incorporation of natural sample (i.e. ice core) observations, which can then be compared with Ground Penetrating Radar (GPR) and seismic observations, in order to provide correlation between observed and modeled data.

SeidarT's architecture is designed to be open and extensible, making it easy to integrate with additional Python packages or even other scripting languages as needed. The design philosophy follows a modular and flexible approach to cater to a wide range of geophysical applications and user skill sets. The core of the software is built around the staggered grid finite difference time domain (FDTD) method, which provides robust and accurate solutions for 4th order seismic and 2nd order electromagnetic wave propagation.

Models are organized in a JSON (JavaScript Object Notation) file [Bray (2017)] where users can define domain parameters, source locations, and the properties associated with the materials present within the domain. The use of JSON provides a readable platform, and this approach streamlines the setup and management of simulations, making it straightforward to configure and run their models.

2.2 Workflow

Building and creating a wave propagation model follows simple image plus JSON workflow (Fig. 1). A rectangular grid, represented by a PNG image establishes the simulation domain where each pixel corresponds to an FDTD node, and each color is assigned an integer ID. These IDs are later referenced in the configuration of the model in order to link material properties and wave parameters to regions in the grid. With the PNG defined, the user creates a JSON project file specifying domain attributes (dimensions, resolution), material settings (e.g., stiffness or permittivity and conductivity tensors), and model parameters (seismic or electromagnetic mode). Tensors can be supplied explicitly or generated, and for 2.5D simulations the x–z plane properties are extruded in the y-direction with corresponding CPML settings.

https://doi.org/10.5194/egusphere-2026-1357
Preprint. Discussion started: 31 March 2026

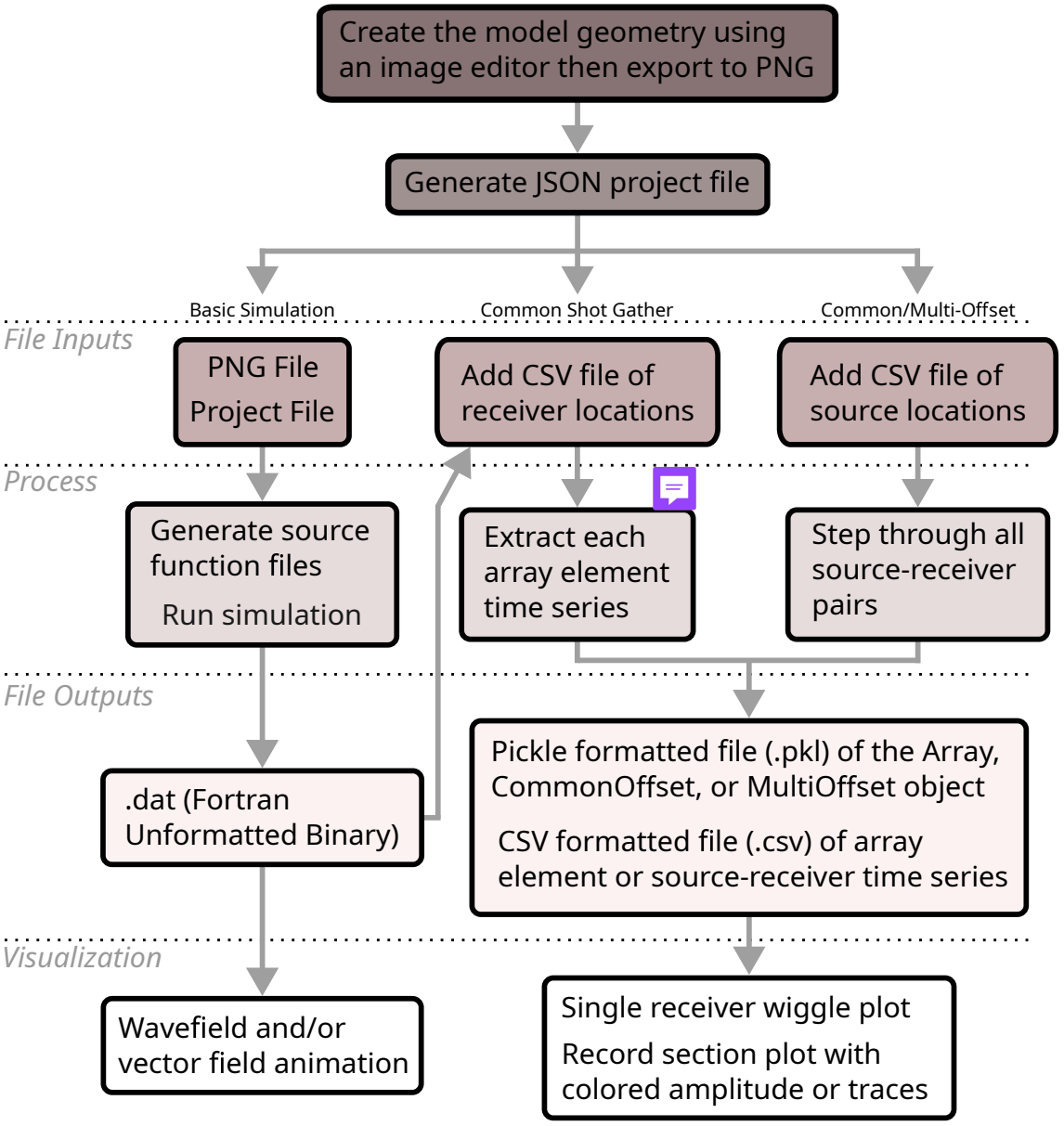

Figure 1. The general workflow tree for creating a wave propagation model and survey simultations. All of the simulations are supersets of the basic simulation. The common shot gather can be built post run making it possible to build different array configurations without rerunning the model.

https://doi.org/10.5194/egusphere-2026-1357
Preprint. Discussion started: 31 March 2026

Only two files are strictly required to run a simulation: the JSON project file and the PNG image. At build time, the user specifies at least the number of time steps and source center frequency, and may optionally define initial conditions. *SeidarT* automatically checks that the source frequency, grid spacing, and velocity model satisfy a Courant–Friedrichs–Lewy (CFL) condition and chooses a stable time step (Courant et al., 1928). The default CFL of 0.707 can be adjusted when stricter stability is needed. Default CPML parameters are also generated but can be overridden to tune boundary performance. Simulation outputs are written as Fortran unformatted binary files (`.dat`) at each time step. Although this increases storage, it preserves the full wavefield, allowing post hoc construction of arbitrary receiver arrays and extraction of particle-velocity or electric-field time series at any node, including dense virtual-sensor networks.

SeidarT supports common-offset profiling by extending internal class variables to generate series of model runs. For common-offset surveys, a CSV file specifies paired source and receiver locations, with each row containing a source–receiver pair. Results from common shot gathers and common-offset surveys can be exported as pickle-formatted files and/or CSV files. Pickle files retain model parameters, time series, and derived products within a single object, while CSV output facilitates import into external signal-processing workflows. Receiver geometry for common-offset surveys is fixed for a given run, so changing array layout requires rerunning the survey, but the modular design makes it straightforward to set up, rerun, and analyze different acquisition scenarios.

https://doi.org/10.5194/egusphere-2026-1357
Preprint. Discussion started: 31 March 2026

3 Computational Framework

3.1 Governing Equations

Wave propagation refers to the manner in which elastic (seismic) or electromagnetic perturbations travel through complex, often heterogeneous materials. Accurately capturing those waves—especially in anisotropic or attenuating media—requires a discretization strategy that resolves both fine-scale interfaces and broad-scale structures. While finite-element (FEM) and spectral-element (SEM) methods offer high accuracy per degree of freedom, they introduce substantial implementation complexity and often rely on external libraries. By contrast, a finite-difference time-domain (FDTD) approach, though computationally heavier, remains remarkably minimalist: it directly discretizes Maxwell's equations (for EM) or the elastodynamic equations (for seismic) on a simple Cartesian grid. This simplicity makes the codebase easier to inspect, modify, and extend.

The FDTD approach has undergone continuous refinement to handle increasingly complex media and boundary conditions. Maxwell's equations or the equations of motion can be discretized using a grid where the electric and magnetic field (or stress and velocity) components are staggered in both space and time. The early work of Virieux (1984) laid a strong foundation with the development of velocity-stress finite-difference methods for horizontal shear wave propagation. By introducing a staggered-grid formulation, Virieux was able to discretize both velocity and stress without artificially smoothing internal boundaries, computing each component so that it is centered between neighboring components. During each time step, the velocity from the previous step is first used to update the current stress, and this updated stress is then used to compute the current velocity before advancing to the next time step. His method was based on the first-order hyperbolic system for SH-wave propagation and became the prototype for many later FDTD schemes.

Implementation of Maxwell's equations and the elastic wave equation follow similar approaches and we will lay out both sequentially. To derive the staggered-grid formulation, we start from the continuous constitutive relations that couple stress to particle velocity in an elastic medium. The generalized form for the constitutive equations of motion (Lai et al., 2009) is

$$\sigma_{ij,t} + \gamma_{ij}\sigma_{ij} = \frac{\mathbb{C}_{ijkl}(u_{k,lt} + u_{l,kt})}{2} + S_{ij}(\mathbf{x}, t) \tag{1}$$

(2)

$$\rho u_{i,tt} = \sigma_{ji,j} + F_i^{(s)}, \tag{3}$$

where $\boldsymbol{\sigma}$ is the Cauchy stress tensor, $\mathbb{C}$ is the 4th-order stiffness tensor, ρ is the density, $\mathbf{u}$ is displacement, and $\boldsymbol{\gamma}$ describes viscoelastic attenuation. Sources are prescribed either as stress-type moment-tensor terms (e.g., double couple, CLVD, explosive)

$$S_{ij}(\mathbf{x}, t) = M_{ij} w(t) \delta(\mathbf{x} - \mathbf{x}_s), \tag{4}$$

where M_{ij} is the moment tensor and $\delta(\mathbf{x} - \mathbf{x}_s)$ denotes a point source at location $\mathbf{x}_s$, or as equivalent body forces

$$F_i^{(s)}(\mathbf{x}, t) = \rho \hat{e}_i w(t) \delta(\mathbf{x} - \mathbf{x}_s), \tag{5}$$

https://doi.org/10.5194/egusphere-2026-1357
Preprint. Discussion started: 31 March 2026

with $\hat{e}_i$ the i-th unit basis vector. The source wavelet $w(t)$ may be chosen from a range of user-defined functions (e.g., Gaussian pulse, Ricker, higher-order Gaussian derivatives, multi-modal sweeps, chirps), allowing the incident spectrum and time–frequency content to be tailored to a given application. Finite-difference expansions of Eqs. (2)–(3) follow standard staggered-grid formulations (Virieux, 1984), and in *SeidarT* we employ a 2nd-order stencil on the staggered grids to obtain an overall 4th-order scheme in space.

The finite difference expansion of Eqs. (2) and (3) are relatively straightforward at this point and can be referred to in more detail in Virieux (1984). This approach ensured that both the stress and velocity fields are modeled in heterogeneous media with a minimum of second-order accuracy in both time and space. We have applied a 2nd order finite difference stencil to both grids to provide a 4th order modeling scheme.

Attenuation is modeled through the amplitude decay of a wave traveling distance d from a directional source with initial amplitude $\mathbf{A}_0$ (Aki and Richards, 2002):

$$\mathbf{A} = \mathbf{A}_0 e^{-\boldsymbol{\alpha} d}, \tag{6}$$

where $\boldsymbol{\alpha}$ is a second order tensor with components, applied component-wise in a chosen coordinate frame,

$$\alpha_{ij} = \frac{\pi f}{c Q_{ij}} = \frac{\gamma_{ij}}{c}. \tag{7}$$

Here f is frequency, c is phase velocity, and $\mathbf{Q}$ is the quality factor, which is often treated as frequency independent over limited bandwidths (Kjartansson, 1979; Gusmeroli et al., 2010a; Agnew et al., 2023). In the most general case, the attenuation tensor $\boldsymbol{\gamma}$ is 4th-order and couples relaxation of all stress components. For computational efficiency and stability, we assume component-wise relaxation and reduce $\boldsymbol{\gamma}$ to a 2nd-order tensor while retaining the ability to represent direction- and mode-dependent attenuation in the materials of interest.

Electromagnetic wave propagation is described by a parallel structure governed by Maxwell's equations (Chew, 1999; Roden and Gedney, 2000). Faraday's law,

$$\epsilon_{ijk} E_{k,j} = -\mu_{il} H_{l,t}, \tag{8}$$

relates spatial gradients of the electric field $\mathbf{E}$ to temporal changes in the magnetic field $\mathbf{H}$, where ϵ_{ijk} is the Levi-Civita symbol and μ is the magnetic permeability. Ampère's law for a lossy medium,

$$\epsilon_{ijk} H_{k,j} - \sigma_{ij} E_j + \varepsilon_{ij} E_{j,t} = \mu_{ij} J^0_j, \tag{9}$$

introduces the conductivity tensor $\boldsymbol{\sigma}$, permittivity tensor $\boldsymbol{\varepsilon}$, and source term $\mathbf{J}^0$, which is treated analogously to the body-force source in Eq. (5). For many non-magnetic materials and in air–ice–water mixtures relevant to cryospheric studies, magnetic permeability is close to unity, so we set $\mu = 1$ without loss of generality.

The numerical implementation of electromagnetic wave propagation and seismic wave propagation follows very similar approaches. While the equations of motion and Maxwell's equations describe different physical phenomena, they share structural similarities since they are both systems of partial differential equations; thus, they can be decomposed similarly into their

https://doi.org/10.5194/egusphere-2026-1357
Preprint. Discussion started: 31 March 2026

respective finite-difference approximations. The primary difference between them is the material properties (i.e. stiffness and permittivity) that relate the stress and velocity fields or the electric and magnetic fields.

3.2 Absorbing Boundary

To suppress spurious reflections from the model edges, *SeidarT* uses a Convolutional Perfectly Matched Layer (CPML) formulation for both seismic and electromagnetic simulations, following Roden and Gedney (2000) and subsequent extensions to complex and anisotropic media (Komatitsch and Martin, 2007; Martin et al., 2008a; Martin and Komatitsch, 2009). This provides robust absorption for grazing, low-frequency, and anisotropically propagating waves on Cartesian grids. In practice, users typically rely on default CPML parameters tuned as a function of source frequency and grid spacing, but the underlying formulation allows manual control of stretching, conductivity, and frequency-shift terms when more aggressive damping or nonstandard geometries are required. Full expressions for the CPML coefficients, implementation details, and recommended parameter ranges for anisotropic ice and snow are provided in Appendix B1.

3.3 Stability Conditions

Time stepping in *SeidarT* is constrained by two standard stability conditions for explicit FDTD schemes. First, a Courant–Friedrichs–Lewy (CFL) condition limits the time step so that waves do not propagate more than one grid cell per step, with a default Courant number chosen to be safe for 2D and 2.5D elastic and electromagnetic problems. Second, a wavenumber band-limit criterion constrains the maximum spatial step relative to the minimum phase velocity and dominant source frequency to avoid spatial aliasing and dispersion of the shortest wavelengths. In the main workflow, SeidarT automatically checks these conditions, computes a stable time step, and warns the user when grid spacing is too coarse; derivations and parameter choices are summarized in Appendix B2.

3.4 Orientation

Given a specific crystal system (i.e cubic, hexagonal, etc.) many of the terms in Eq. (2) are zero due to coefficients in $\mathbb{C}$ being zero. However, anisotropy, heterogeneities, and preferred crystal orientation fabrics (PCOF) have been observed in glacier systems and are shown to have significant impacts on the flow dynamics of glaciers [i.e. (Alley, 1988; Riche et al., 2013; Gerbi et al., 2021; Hellmann et al., 2021; Monz et al., 2021)], therefore we consider the bulk effective medium of snow and ice in our numerical implementation which, as a circumstance, produces stiffness tensors that exhibit lower symmetry.

For reasons of being computationally fast and easy to implement while maintaining an acceptable degree of accuracy (Berryman, 1995), we use the Hill average which is the arithmetic mean from the Voigt (Voigt, 1910) and Reuss (Reuß, 1929) upper and lower bounds, respectively, in order to calculate the bulk effective medium (Hill, 1952; Man and Huang, 2011). For second order tensor, as seen in the electromagnetic constitutive equations [Eqs. (8) and (9)], we can compute the bulk permittivity and conductivity tensors from rotation matrices derived from the Euler angles - ϕ, θ, ψ.

https://doi.org/10.5194/egusphere-2026-1357
Preprint. Discussion started: 31 March 2026

The orientation of a crystal relative to a reference coordinate system can be described by a rotation matrix. A rotation matrix can be formed in a variety of ways (e.g. roll, pitch, yaw), but for simplicity and commonality we can consider the Bunge ($z-x-z$) Euler angle rotation (Bunge, 2013). For the rotation about each of the three axes for a given angle θ we have

$$\mathbf{R}_x(\theta) = \begin{bmatrix} 1 & 0 & 0 \\ 0 & \cos\theta & -\sin\theta \\ 0 & \sin\theta & \cos\theta \end{bmatrix}, \quad \mathbf{R}_y(\theta) = \begin{bmatrix} \cos\theta & 0 & \sin\theta \\ 0 & 1 & 0 \\ -\sin\theta & 0 & \cos\theta \end{bmatrix} \mathbf{R}_z(\theta) = \begin{bmatrix} \cos\theta & -\sin\theta & 0 \\ \sin\theta & \cos\theta & 0 \\ 0 & 0 & 1 \end{bmatrix}, \tag{10}$$

therefore, the $z-x-z$ rotator is matrix product of the three rotation matrices of 3 independent angles

$$\mathbf{R}(\phi,\theta,\psi) = \mathbf{R}_z(\phi)\mathbf{R}_x(\theta)\mathbf{R}_z(\psi). \tag{11}$$

and rotation of a 3×3 tensor follows as

$$\mathbf{T}' = \mathbf{R}\mathbf{T}\mathbf{R}^\top. \tag{12}$$

Thus we can compute the Voigt and Reuss tensors, $\mathbf{T}_{\text{Voigt}}$ and $\mathbf{T}_{\text{Reuss}}$ approximations from

$$\mathbf{T}_{\text{Voigt}} = \frac{1}{n}\sum_{i=1}^{n} f_i \mathbf{T}_i \tag{13}$$

$$\mathbf{T}^{-1}_{\text{Reuss}} = \frac{1}{n}\sum_{i=1}^{n} f_i \mathbf{T}_i^{-1} \tag{14}$$

$$\mathbf{T}_{Hill} = \frac{\mathbf{T}_{Voigt} + \mathbf{T}_{Reuss}}{2} \tag{15}$$

where f is the fractional volume of the crystal (Voigt, 1910; Reuß, 1929; Bunge, 2013).

For a 2nd order tensor such as the permittivity tensor, rotation and bulk effective estimation, Eq (12-15) can easily be applied. However, rotation of the stiffness tensor requires a few additional steps to compute bulk effective estimates. For a 6×6 matrix rotation such as those required for the stiffness and compliance tensor, it can be shown that

$$\mathbb{C}_{ijkl} = \mathbf{R}_{ip}\mathbf{R}_{jq}\mathbf{R}_{kr}\mathbf{R}_{ls}\mathbb{C}_{pqrs} \tag{16}$$

although, for brevity, we will revert to the simplification from Bond (1943) who provided a more computationally efficient and concise description of the rotation matrix needed for a 6×6 rotation. The Bond matrix is thus written as

$$\mathbf{B} = \begin{bmatrix} R_{11}^2 & R_{12}^2 & R_{13}^2 & 2R_{12}R_{13} & 2R_{13}R_{11} & 2R_{11}R_{12} \\ R_{21}^2 & R_{22}^2 & R_{23}^2 & 2R_{22}R_{23} & 2R_{23}R_{21} & 2R_{21}R_{22} \\ R_{31}^2 & R_{32}^2 & R_{33}^2 & 2R_{32}R_{33} & 2R_{33}R_{31} & 2R_{31}R_{32} \\ R_{21}R_{31} & R_{22}R_{32} & R_{23}R_{33} & R_{22}R_{33}+R_{23}R_{32} & R_{21}R_{33}+R_{23}R_{31} & R_{22}R_{31}+R_{21}R_{32} \\ R_{31}R_{11} & R_{32}R_{12} & R_{33}R_{13} & R_{12}R_{33}+R_{13}R_{32} & R_{13}R_{31}+R_{11}R_{33} & R_{11}R_{32}+R_{12}R_{31} \\ R_{11}R_{21} & R_{12}R_{22} & R_{13}R_{23} & R_{12}R_{23}+R_{13}R_{22} & R_{13}R_{21}+R_{11}R_{23} & R_{11}R_{22}+R_{12}R_{21} \end{bmatrix}, \tag{17}$$

https://doi.org/10.5194/egusphere-2026-1357
Preprint. Discussion started: 31 March 2026

Likewise, for the rotation of the compliance matrix, as a consequence of the properties of orthogonal matrices, we can avoid computing the inverse and simply apply the transpose inverse bond matrix, $\mathbf{N}$, such that

$$\mathbb{S}' = \mathbf{N}\mathbb{S}\mathbf{N}^{\top} \tag{18}$$

where $\mathbb{S} = \mathbb{C}^{-1}$ is the compliance matrix.

Estimating the isotropic tensor from a single anisotropic crystal can follow two approaches. One method involves applying rotations from Euler angles to generate a large population of crystal orientations, which must reach extremely high numbers to effectively converge to the isotropic case. However, this approach is computationally intensive and can be approximated more efficiently. For a transversely isotropic material, the shear and bulk moduli can be extracted directly from the stiffness coefficients. Under the Voigt approximation, the effective shear modulus is simply the arithmetic mean of the shear components c_{44} and c_{66}, while the effective bulk modulus is given by (deWit, 2008)

$$K_{Voigt} = c_{11} + c_{12} + 2c_{13} + 2c_{33} + 2c_{44}/6. \tag{19}$$

Similarly, the Reuss effective shear and bulk moduli can be calculated from the compliance tensor.

3.4.1 Permittivity of Ice and Snow

For a pure, single crystal of ice, the real permittivity can first be related to its density, ρ (in $\mathrm{kg \cdot m^{-3}}$, via the empirical fit of Kovacs et al. (1995)

$$\varepsilon = (1 + 0.845 \cdot \rho)^2 \tag{20}$$

At microwave and higher frequencies, however, ice is a lossy dielectric, and its permittivity must be treated as a complex quantity (Fujita et al., 1993, 2000; Matsuoka et al., 2012)

$$\varepsilon^* = \varepsilon' - j\varepsilon'' \tag{21}$$

Because ice is anisotropic (hexagonal crystal), the complex permittivity takes a diagonal tensor form in the crystal coordinate frame, with one value parallel to the c-axis and one perpendicular

$$\varepsilon = \begin{bmatrix} \varepsilon^*_{\perp} & 0 & 0 \\ 0 & \varepsilon^*_{\perp} & 0 \\ 0 & 0 & \varepsilon^*_{\parallel} \end{bmatrix} \tag{22}$$

The real part ε' shows a slight, nearly linear increase with temperature, T (in ^{o}C) (Fujita et al., 1993)

$$\varepsilon' = 3.1884 + 9.1 \cdot 10^{-4} \cdot T. \tag{23}$$

The difference in the extraordinary-ordinary real permittivity, $\Delta\varepsilon' = \varepsilon'_{\parallel} - \varepsilon'_{\perp}$, is temperature dependent with the following relationship (Fujita et al., 1993)

$$\Delta\varepsilon'(T) = 0.0256 \pm 0.00137 + 3.57 \cdot 10^{-5}(6.0 \cdot 10^{-6})T \tag{24}$$

https://doi.org/10.5194/egusphere-2026-1357
Preprint. Discussion started: 31 March 2026

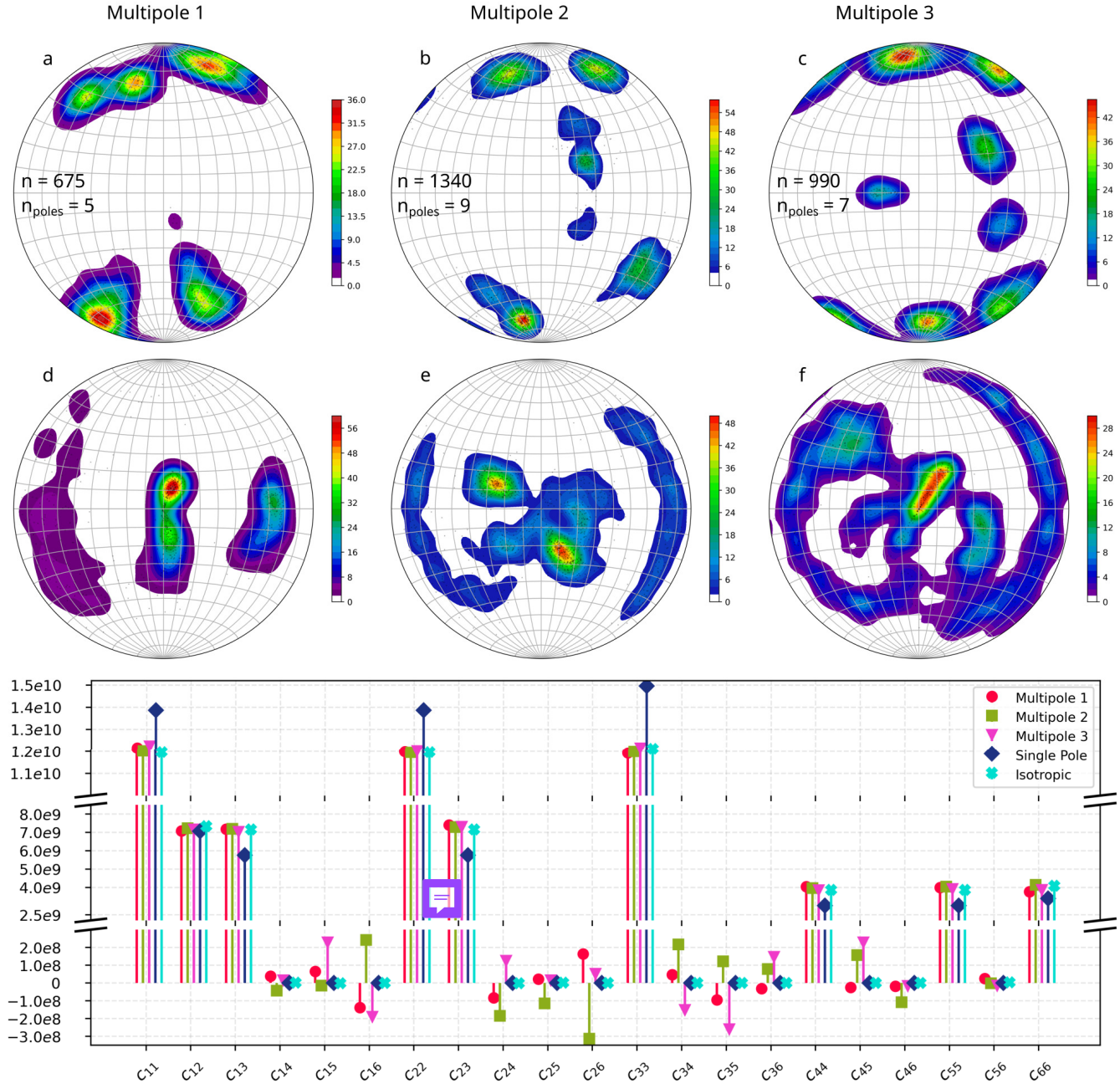

Figure 2. Stereonet plots to simulate the microstructures found in Monz et al. (2021). Both the c-axes (a-c) and a-axes (d-f) were generated using parameterized normal distributions. The stem chart in the lower plot shows stiffness coefficients, c_{ij}, which were estimated from the Hill average (Eq. 15) for each microstructure for non-porous, anhydrous ice at -5 ^{o}C. The y-axes limits are piece wise with different magnitude ranges, and the single pole stiffness coefficients for a transversely isotropic single ice-1h crystal (blue diamond) and isotropic fabric (cyan x) can be seen for reference. The stiffness coefficients for the microstructures appear to be isotropic, however the non-zero values in the upper right and lower left block of the stiffness tensor show a more complex relationship between the shear strain and normal stress as well as the normal strain and shear stress. All stiffness tensors are positive definite.

https://doi.org/10.5194/egusphere-2026-1357
Preprint. Discussion started: 31 March 2026

Computing the imaginary part of the permittivity - Fujita et al. (2000) solved the following set of equations based on data from Jiracek (1967)

$$\varepsilon''(T) = \frac{A(T)}{f} + B(T) f^{C(T)} \tag{25}$$

such that A describes Debye relaxation, the second term containing B and C corresponds to infrared absorption.

When moving from the simple case of a single ice crystal to the naturally occurring polyphase material of ice found in snowpacks, the complexity of electrical permittivity increases substantially. Snow often incorporates air pockets and liquid water inclusions among an ice matrix, and as a result, depends on key physical parameters. Among these are the liquid water content (LWC), the dry snow density (ρ_d) and the temperature (T) of the material.

Multiple models have been developed to quantify the dependence of permittivity on these factors. From Tiuri et al. (1984), we have the expression for the real permittivity

$$\varepsilon = 8.8 \cdot LWC + 70.4 \cdot LWC^2 + 1 + 1.17 \cdot \rho_d + 0.7 \cdot \rho_d^2 \tag{26}$$

which incorporates both linear and quadratic terms in the LWC and ρ_d, highlighting their non-linear influence on permittivity. The corresponding expression for the loss factor (imaginary component), accounting for frequency dependence, was empirically derived as: and the complex permittivity

$$\varepsilon'' = \frac{f}{10^9}\left(0.9 \cdot LWC + 0.72 \cdot LWC^2\right) \tag{27}$$

Similarly, according to the Wise Snow Liquid Water Content Sensor User Manual [A2 Photo Sensors (2019)

$$\varepsilon = 1 + 1.202 \cdot \rho_d + 0.983 \cdot \rho_d^2 + 21.4 \cdot LWC. \tag{28}$$

The permittivity of snow near its melting point becomes dominated by the presence of liquid water. Measuring the liquid water content *in situ* can be challenging due to technical limitations and complexities involved. To address this, alternative models have been proposed that relate permittivity directly to temperature making it much easier to measure precisely. Liebe et al. (1991) provides us with:

$$\varepsilon = 77.66 - 103.3 \cdot \left(1 - \frac{300}{T}\right) \tag{29}$$

allowing temperature to serve as a proxy for the influence of water within the snow pack. Expanding on this, Jones and Or (2005) formulated a higher-order temperature-dependent model

$$\varepsilon = 78.51 \cdot (1 - 4.579 \cdot 10^{-3} \cdot (T - 298) + 1.19 \cdot 10^{-5} \cdot (T - 298)^2 - 2.8 \cdot 10^{-8} \cdot (T - 298)^3 \tag{30}$$

enabling accurate prediction of permittivity across a wider thermal range without direct liquid water content measurement.

Eqs. 26 and 27 are incoroporated as the default because they account for both the real and imaginary components. To ensure accurate treatment of liquid water contributions, temperature co ions are applied to the density of water using the well-established Kell equation (Kell, 1975).

https://doi.org/10.5194/egusphere-2026-1357
Preprint. Discussion started: 31 March 2026

3.4.2 Ice Stiffness

The stiffness coefficients for a single ice crystal are presented by Gagnon et al. (1987) with units in bars as:

$$c_{11}(P,T) = 148.389 + 4.7546P - 1.1307 \cdot 10^{-1}P^2 - 2.8941 \cdot 10^{-1}T - 1.7827 \cdot 10^{-3}T^2 \quad (31)$$

$$c_{12}(P,T) = 72.639 + 7.2109P - 3.7096 \cdot 10^{-1}P^2 - 1.4673 \cdot 10^{-1}T - 9.0362 \cdot 10^{-4}T^2 \quad (32)$$

$$c_{13}(P,T) = 61.445 + 8.4732P - 4.2016 \cdot 10^{-1}P^2 - 1.1916 \cdot 10{-}1T - 7.3120 \cdot 10^{-4}T^2 \quad (33)$$

$$c_{33}(P,T) = 157.960 + 2.8083P - 1.2510 \cdot 10^{-1}P^2 - 3.112910^{-2} - 1.8948 \cdot 10^{-3}T \quad (34)$$

$$c_{44}(P,T) = 29.490 - 1.5055P - 1.2677 \cdot 10^{-2}P^2 - 6.2874 \cdot 10^{-2} - 3.8956 \cdot 10^{-4}T \quad (35)$$

and by Petrenko and Whitworth (1999) such that

$$c_{11} = 11.0 - 0.05 \cdot T + 0.4 \cdot P \quad (36)$$

$$c_{12} = 5.0 - 0.03 \cdot T + 0.3 \cdot P \quad (37)$$

$$c_{13} = 4.5 - 0.03 \cdot T + 0.35 \cdot P \quad (38)$$

$$c_{33} = 11.5 - 0.05 \cdot T + 0.5 \cdot P \quad (39)$$

$$c_{44} = 3.2 - 0.02 \cdot T + 0.1 \cdot P. \quad (40)$$

(41)

Density of a single ice crystal in relation to the stiffness values in Eq (35) can be written in two equivalent forms. First, a simple thermal-expansion law,

$$\rho(T) = \rho_o(1 - \beta T) \quad (42)$$

with $\beta = 51 \cdot 10^{-6o}$C. Or combining pressure and temperature effects explicitly,

$$\rho(P,T) = 922.15 + 10.28 \cdot 10^{-2}P - 0.2503 \cdot 10^{-4}P^2 - 0.1445T + 2.77 \cdot 10^{-4}T^2 \quad (43)$$

These expressions can serve as a basis for individual grains in crystal fabrics, homogeneous ice, or polyphase (i.e. snow) and polymineralic conglomerates that include ice crystals sediment entrained ice).

3.4.3 Snow Stiffness

In contrast to consolidated ice or rock - where the microstructure is relatively uniform and connectivity assumptions hold - materials such as snow exhibit highly variable porosity, grain contact networks, and liquid-water saturation (Schneebeli and Sokratov, 2004; Calonne et al., 2011). As temperature and melt conditions fluctuate, the ice skeleton can transition from a continuous framework to isolated granule foam-like structures which invalidate some of the assumptions that make the aforementioned averaging inaccurate. Consequently, estimating the effective stiffness of snow requires an appropriate selection of a homogenization method that accounts for both solid-matrix connectivity and pore-fluid effects.

https://doi.org/10.5194/egusphere-2026-1357
Preprint. Discussion started: 31 March 2026

For modeling snow stiffness from its polyphase constituents - ice, water, and air - the choice between the Hill estimate and other averaging schemes such as Gassmann's equations or the Self-Consistent Approximation (SCA) depends on porosity and liquid water content. The Hill estimate (Hill, 1952) is suitable for moderate porosity (typically $\leq 50\%$) where the ice matrix remains connected, providing an average of the Voigt and Reuss bounds. Gassmann's equations (Gassmann, 2007) apply when the pore space is highly saturated (typically above 80% liquid water content), assuming a connected pore fluid network that primarily affects bulk modulus while leaving the shear modulus unchanged.

For high porosity conditions (greater than or equal to 50%), where the ice skeleton becomes largely disconnected, SCA (Berryman, 1980) is better suited because it explicityly represents snow as a granular or foam-like composite. In this regime, SCA provides a more realistic estimate of the effective stiffness tensor than simple Voigt-Reuss averaging by accounting for the loss of frame connectivity and the mechanical contrast between ice and the pore phase. Choosing an appropriate homogenization scheme is therefore essential for predicting effective stiffness in a way that is consistent with both microstructural connectivity and fluid saturation.

To parameterize these models, we first define the bulk modulus of the pore fluids - water and air - as functions of temperature T (and, for air, pressure), since these moduli enter directly into both the dry-frame scaling and the Gassman fluid substitution. The bulk modulus of water is expressed as a function of temperature T, with separate polynomial fits for the liquid state and the supercooled regime:

$$K_{\text{water}}(T) = \begin{cases} 2.15 - 0.0164T + 4.72 \times 10^{-5}T^2 - 6.5 \times 10^{-7}T^3, & 0 \leq T \leq 100 \\ 2.25 - 0.016T - 6.9 \times 10^{-5}T^2, & -30 \leq T < 0, \end{cases} \tag{44}$$

while the bulk modulus of air is estimated from its thermodynamic properties as

$$K_{\text{air}}(T, P) = \gamma_{\text{adi}} \cdot \rho_{\text{air}} \frac{RT}{M} \tag{45}$$

with the air density

$$\rho_{air}(T, P) = \frac{PM}{RT}, \tag{46}$$

where P is the pressure, R is the ideal gas constant, M is the molar mass, and γ_{adi} is the adiabatic index. Given $\rho_{air} = P/(RT)$, the adiabatic sound speed simplifies to $c = \sqrt{\gamma_{\text{adi}} RT}$, making termperature a key control on wave speeds in air-filled pore space even when pressure is fixed.

Gassmann's equation for the saturated bulk modulus is given by:

$$K_{\text{sat}} = K_{\text{dry}} + \frac{\left(1 - \frac{K_{\text{dry}}}{K_{\text{mineral}}}\right)^2}{\frac{\phi}{K_{\text{fluid}}} + \frac{1-\phi}{K_{\text{mineral}}} - \frac{K_{\text{dry}}}{K^2_{\text{mineral}}}} \tag{47}$$

where K_{dry} is the bulk modulus of the dry snow matrix, K_{mineral} is the bulk modulus of the solid mineral (ice), K_{fluid} is the bulk modulus of the saturating fluid, and ϕ is the porosity. Gassmann's relation assumes that the saturating fluid is homogeneously distributed, the pore structure is well-connected, and that the solid grains are significantly stiffer than the pore fluid.

https://doi.org/10.5194/egusphere-2026-1357
Preprint. Discussion started: 31 March 2026

In our implementation, the dry frame modulus is estimated by scaling the ice modulus as

$$K_{\text{dry}} = K_{\text{ice}}(1-\phi)^n, \tag{48}$$

with an exponent n (typically tuned between 2 and 5) that controls the reduction in stiffness with increasing porosity. A similar scaling is applied to the shear modulus to obtain a dry shear modulus G_{dry}.

The Self-Consistent Approximation (SCA) models the porous medium as a two-phase composite, where the pores (typically filled with a much softer material such as air) are embedded in a continuous ice matrix. The effective stiffness tensor, $\mathbb{C}_{\text{eff}}$, is determined by considering the interaction between the inclusions (pores) and the matrix. A key component in this framework is the Eshelby tensor, $\mathbf{S}$, which characterizes the influence of an isolated, ellipsoidal inclusion on the surrounding matrix Eshelby and Peierls (1957). For spherical inclusions (aspect ratio equal to 1), the Eshelby tensor in Voigt notation is given by

$$\mathbf{S} = \begin{bmatrix} \frac{3}{8}\mathbf{I} & 0 \\ 0 & \frac{1}{4}\mathbf{I} \end{bmatrix}, \tag{49}$$

where $\mathbf{I}$ is the 3×3 identity matrix.

The effective stiffness is obtained by iteratively solving a self-consistent relation. Let $\mathbb{C}_{\text{matrix}}$ denote the stiffness tensor of pure ice and $\mathbb{C}_{\text{inclusion}}$ that of the pore-filling phase (which is nearly zero for air). If ϕ is the porosity (expressed as a fraction between 0 and 1), then the update equation for the effective stiffness is (Budiansky, 1965; Berryman, 1995)

$$\mathbb{C}_{\text{eff}}^{(k+1)} = \mathbb{C}_{\text{eff}}^{(k)} + \phi\left(\mathbb{C}_{\text{inclusion}} - \mathbb{C}_{\text{eff}}^{(k)}\right)\left[\mathbf{I} + \mathbf{S}\left(\mathbb{C}_{\text{inclusion}} - \mathbb{C}_{\text{eff}}^{(k)}\right)\right]^{-1}, \tag{50}$$

with an initial guess

$$\mathbb{C}_{\text{eff}}^{(0)} = \mathbb{C}_{\text{matrix}}. \tag{51}$$

The iteration is continued until the change satisfies

$$\|\mathbb{C}_{\text{eff}}^{(k+1)} - \mathbb{C}_{\text{eff}}^{(k)}\| < \epsilon, \tag{52}$$

for a prescribed tolerance ϵ.

The self-consistent framework, as further developed by Hill (1965) and Budiansky (1965), provides a means to capture the non-linear reduction in stiffness that occurs as the ice matrix loses connectivity with increasing porosity. Once C_{eff} is determined, the effective bulk modulus K_{eff} and the shear modulus G_{eff} can be derived using standard relationships for isotropic media, and these moduli ultimately determine the seismic velocities (e.g., V_p and V_s) in snow.

Although the Hill estimate simply averages the Voigt and Reuss bounds, it tends to overestimate stiffness in highly porous snow because it does not fully account for the loss of connectivity in the ice skeleton. In such cases, the SCA provides a more realistic estimation of the effective stiffness by iteratively accounting for pore interactions. When the pore space is highly saturated, the Gassmann fluid substitution is applied to update the bulk modulus, while the shear modulus is assumed to remain that of the dry frame. A comparison of the various methods intrinsic to the *SeidarT* software can be seen in Fig. (3).

https://doi.org/10.5194/egusphere-2026-1357
Preprint. Discussion started: 31 March 2026

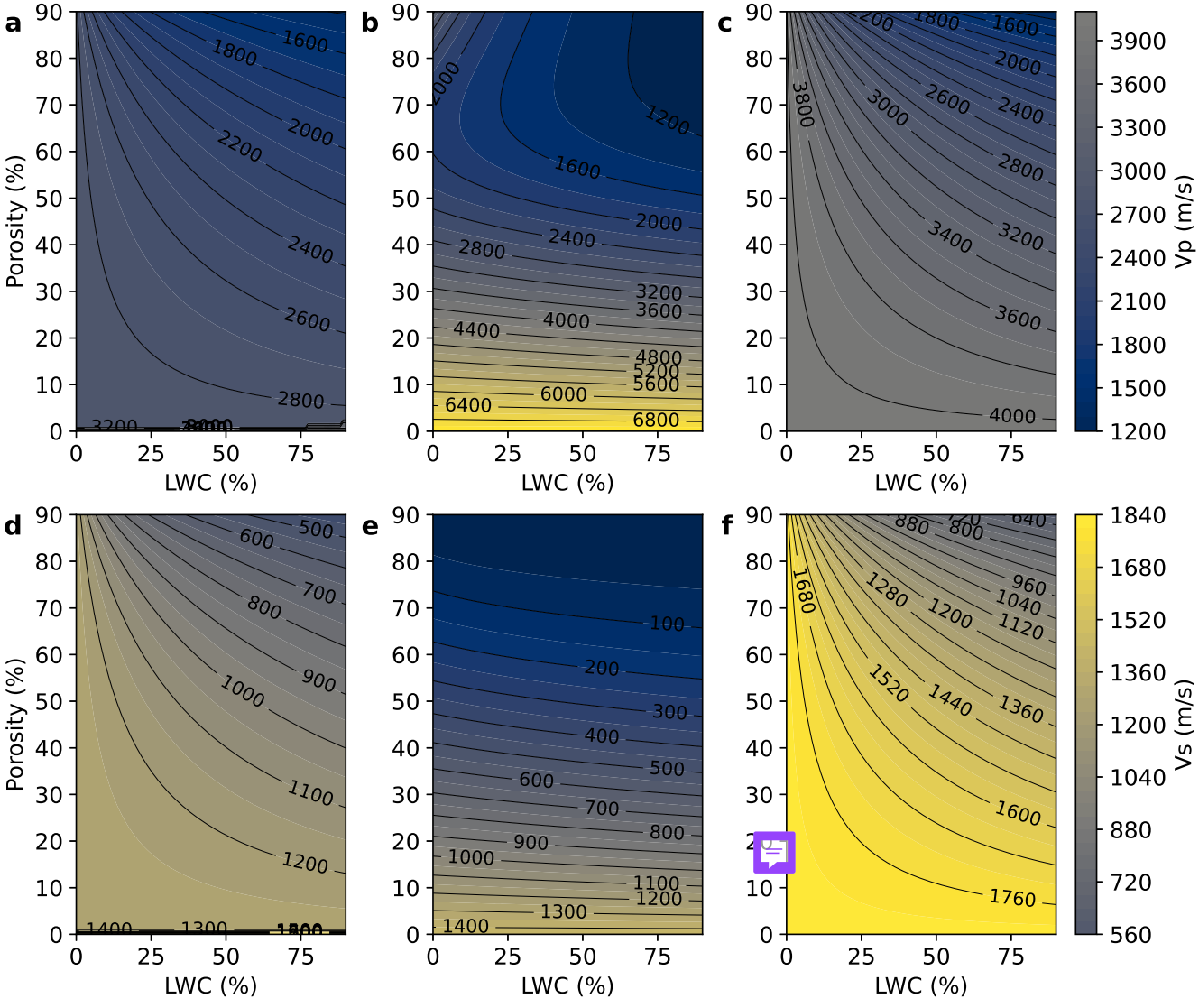

Figure 3. Effective seismic velocities of snow computed at –10°C over a range of porosity (0–90%) and liquid water content (0–90%) using three different homogenization approaches. Top row: vertical (compressional) wave velocity, V_p; bottom row: shear wave velocity, V_s. Columns correspond to (a,d) the Hill average, (b,e) the Gassmann fluid substitution method, and (c,f) the Self-Consistent Approximation (SCA). All panels share common color scales so that identical velocity magnitudes are represented by the same color. While the Hill and SCA methods exhibit the expected decrease in V_p and Vs with increasing porosity and saturation, the Gassmann approach produces higher V_p and anomalous V_s trends. These differences highlight the sensitivity of effective elastic properties to the chosen homogenization technique, which is critical for accurate seismic interpretation in snow-covered and cold-region environments.

https://doi.org/10.5194/egusphere-2026-1357
Preprint. Discussion started: 31 March 2026

To guide model selection, the *SeidarT* software automatically chooses the appropriate homogenization method based on the porosity and liquid water content, though users may override this default and explicitly specify a preferred scheme. For snow with moderate porosity (typically $\phi \leq 50\%$) and limited saturation, the Hill estimate offers a simple and efficient approximation. When liquid water saturation exceeds 80%, indicating a well-connected pore-fluid network, the Gassmann fluid substitution is applied to adjust the bulk modulus accordingly while keeping the shear modulus fixed. In high-porosity conditions ($\phi \geq 50\%$), especially when the ice matrix becomes discontinuous or foam-like, the Self-Consistent Approximation (SCA) is used to more accurately account for the interactions between inclusions and the solid matrix. These thresholds reflect physically meaningful transitions in snow microstructure and ensure that the selected method remains consistent with the dominant mechanical behavior of the medium.

3.5 Fluid Inclusions

For seismic specific modeling, numerical instabilities can occur in regions where there exists high density gradients. This is most commonly observed in the air-surface interface and is due to division by small values. As seen in Eq. (3) the density moves to the right hand side of the equation and becomes part of the denominator in all of the terms. In purely elastic-wave simulations, that boundary is usually handled as a traction-free (free-surface) condition, i.e.

$$\sigma_{zz} = \sigma_{xz} = \sigma_{yz} = 0 \tag{53}$$

However, when modeling fluid- or air-filled cavities deeper within the snowpack (for example englacial air pockets, crevasse voids, or infrasound–seismic coupling problems), the density can be sharply reduced locally in places other than the surface.

Whenever the physical wavelength λ is comparable to—or smaller than—the characteristic size of a cavity, homogenization breaks down and an effective medium approximation is no longer valid. To mitigate this, we replace the sharp discontinuity at the solid/fluid (or solid/air) interface with a smoothed transition zone. Specifically, we apply one of three discrete averaging schemes across the grid cells straddling the boundary. These being: the geometric mean

$$\bar{\rho}_{\text{geo}} = \sqrt{\rho_1 \cdot \rho_2}, \tag{54}$$

the harmonic mean

$$\bar{\rho}_{\text{harm}} = \frac{2\rho_1\rho_2}{\rho_1 + \rho_2} \tag{55}$$

and (3) the arithmetic mean which represents the midpoint between the 2 values.

The geometric mean remains closest to the smaller of the two values and preserves impedence contrast and energy flux across the boundary thus conserving energy. Likewise, the geometric mean is also biased toward the smaller modulus or density, but does not have the same multiplicataive and self-reciprocity that the geometric mean does meaning that it violates the conservation of energy. It yields a transition that is slightly smoother than the geometric mean but still preserves most of the contrast. Meanwhile, the arithmetic mean produces the smoothest variation between solid and fluid/air and is the most stable numerically, but other than violating the conservation of energy, may excessively smear out sharp features. There is

https://doi.org/10.5194/egusphere-2026-1357
Preprint. Discussion started: 31 March 2026

a tradeoff of numerical stability and numerical accuracy when selecting the appropriate gradient method. The choice among these averaging schemes should be guided by the specific modeling objectives whether preserving sharp impedance contrasts is more critical than maximizing numerical stabili r the scenario at hand.

https://doi.org/10.5194/egusphere-2026-1357
Preprint. Discussion started: 31 March 2026

4 Validation

In this section, we demonstrate the accuracy and robustness of our FDTD implementation by systematically validating its key physical outputs, namely travel time predictions, amplitude decay behavior, and full-tensor anisotropic response—against both experimental and analytical benchmarks.

4.1 Electromagnetic

We begin with an electromagnetic zero-offset profile (ZOP) that replicates the zero offset profile survey conducted by Gusmeroli et al. (2010b), verifying that synthetic arrivals and the signal attenuation in Fig (4) are in agreement with the experimental field results.

The vertical profiles of dielectric permittivity provided by Gusmeroli et al. (2010b) showed a layered ice structure with highly attenuative layers, which is deduced to be a result of englacial aquifers or aquitards. The simulation shows a clear reduction in wave velocity and an increase in attenuation below the cold-temperate transition surface (CTS), consistent with the observed increase in water content within the temperate layer. Temperature, radio wave speed, and water content values found in their study can be easily entered into the model framework, but the resulting conductivity estimates were slightly tuned to provide better energy loss behavior in facies with higher water content. We contribute the mismatch in our modeled conductivity values to impurities commonly found in glacier systems.

The ZOP survey of Gusmeroli et al. (2010b) was conducted in water filled boreholes and their effects were corrected for in their observed travel times. Our initial setup included these water filled boreholes but we observed high levels of ringing within them, so we chose to leave them out. This assumption limits our source accuracy and energy coupling, but our simulated waveform amplitudes are in relative agreement with the field-based measurements.

Our results show very similar results to those provided by Gusmeroli et al. (2010b), but there is a slight difference in their interpretation and what we see. They attributed the hyperbola seen propagating from the surface (left side) of the image to be due to reflections from a nearby ablation stake. While we do not dispute this, we see a similar hyperbola forming from the reflection off of the air-ice interface even though our model does not contain an ablation stake.

Next, we illustrate a synthetic 2.5D electromagnetic simulation that incorporates three transversely isotropic media with different degrees of anisotropy: strong (66% - $\varepsilon_{\parallel} = 10$ and $\varepsilon_{\perp} = 2$), moderate (33% - $\varepsilon_{\parallel} = 4$ and $\varepsilon_{\perp} = 2$), and near-isotropic ($< 1\%$ - $\varepsilon_{\parallel} = 3.205$ and $\varepsilon_{\perp} = 3.179$) with the latter being *SeidarT*'s intrinsic values for ice. In all cases, the symmetry axis is confined to the x-y plane and is oriented 45^{o} from the x-axis. The x-direction is defined as zero degrees with positive rotation in the counterclockwise direction. The model is energized by an x-polarized point source, and the plane wave energy is measured as a function of the propagation direction. The source to receiver distance is 21.375m to allow for the development of a polarized plane wave.

The results seen in Fig. (5) show distinct anisotropy-induced polarization effects because the source energy aligns with the symmetry axes. In the high-anisotropy models, electric field energy is preferentially aligned along the fast and slow axes of the material, demonstrating birefringent splitting and directionally dependent energy maxima. In contrast, the near-isotropic (ice)

https://doi.org/10.5194/egusphere-2026-1357
Preprint. Discussion started: 31 March 2026

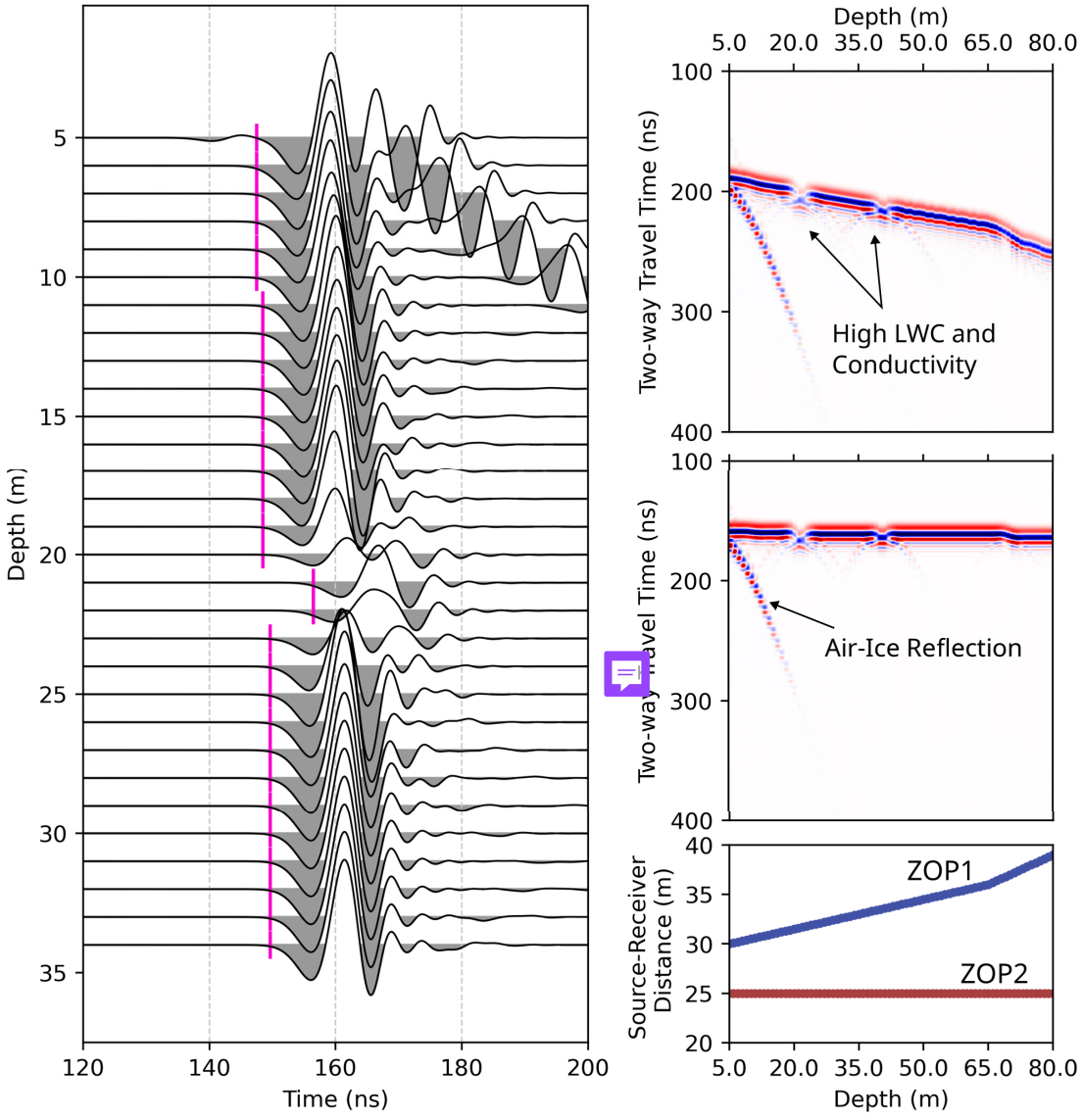

Figure 4. Simulated zero offset profile from parameters gathered by Gusmeroli et al. (2010b). The source was a 100 MHz vertically polarized point source. The theoretical arrival times are seen in the left plot and denoted by the pink lines. The right subplots are reconstructions of the full radar gather profile for the ZOP1 (top) and ZOP2 (center) profiles and their associated source-receiver distances (bottom). The actual source and receiver location for ZOP1 wasn't disclosed so the values were tuned to portray this.

https://doi.org/10.5194/egusphere-2026-1357
Preprint. Discussion started: 31 March 2026

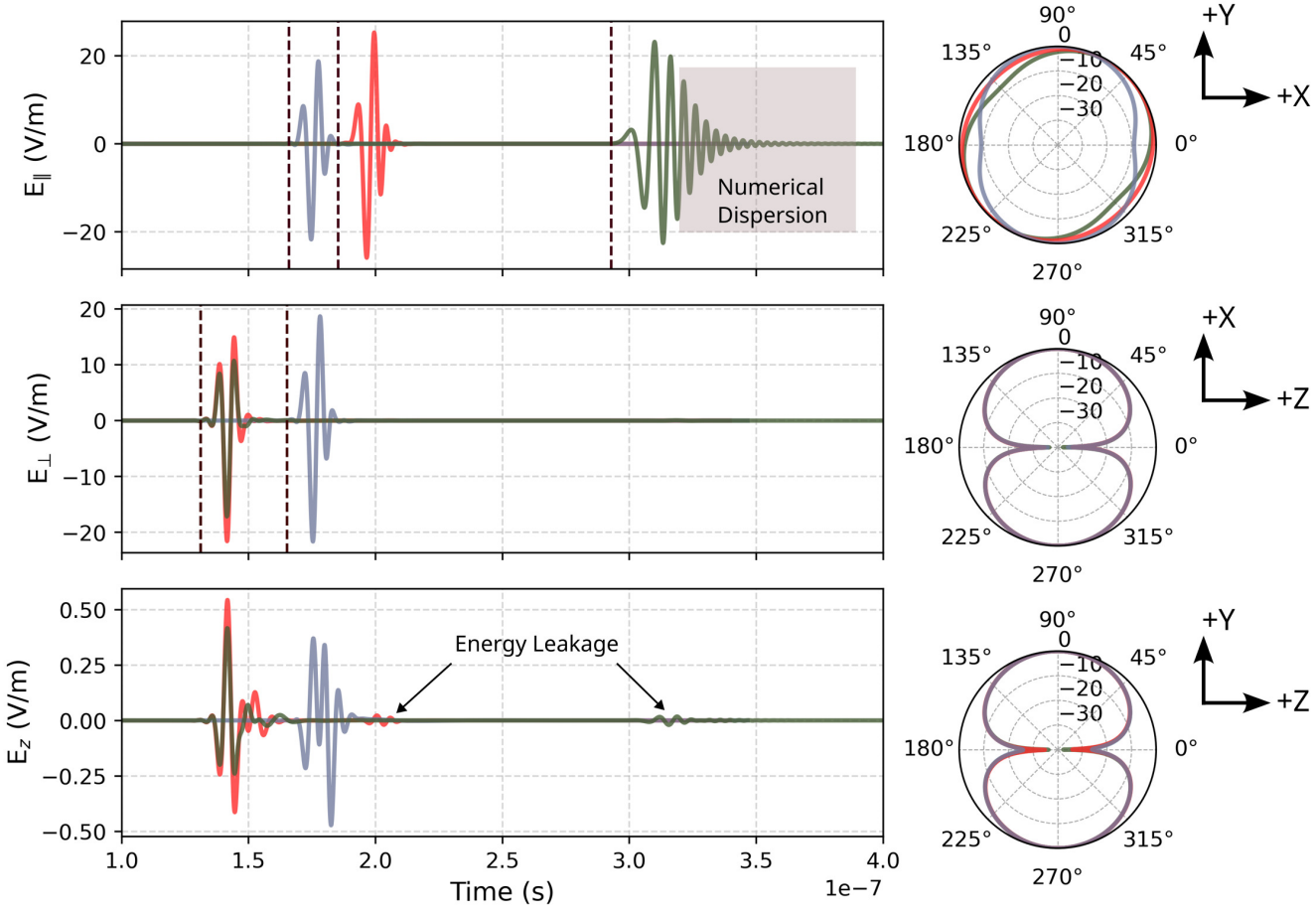

Figure 5. The 3-component plot of the electric fields rotated to show the wave energy for the extraordinary, ordinary, and vertical axes (top to bottom left, respectively) and the plane polarization energy (right) propagating though a transversely isotropic medium. Green is high anisotropy, red is moderate anisotropy, and blue is near isotropic with vertical dashed lines of the expected arrival times. Wave splitting is expected to be evident on the x-y plane which is why all colors are overlayn on the x-z and y-z planes.

https://doi.org/10.5194/egusphere-2026-1357
Preprint. Discussion started: 31 March 2026

Table 1. Layer-wise P- and S-wave velocities and densities for surface and body wave models.

Layer	Surface Wave Model				Body Wave Model			
	V_P (m/s)	V_S (m/s)	ρ (kg/m^3)	h (m)	V_P (m/s)	V_S (m/s)	ρ (kg/m^3)	h (m)
1	343	0	1.4	30	1000	500	1800	10
2	500	287	1800	5	1500	800	1900	20
3	1000	291	1900	10	2000	1100	2000	30
4	1800	989	2000	20	2500	1400	2100	60
5	2522	1300	2200	60	3000	1700	2200	100
6	3500	1575	2400	inf	3500	2000	2300	inf

model exhibits minimal directional dependence, as expected. Some z-polarized leakage is observed across models, particularly in high anisotropy scenarios. This leakage is attributable to the three-dimensional nature of the wavefield and confirms that the solver correctly captures mode conversion and polarization rotation due to anisotropic material properties. The observed numerical dispersion in the high anisotropy model is due to the high contrast in velocities and the difficulty in accommodating the directional dependence into the absorbing boundary. This can be minimized or mitigated by expanding the grid cells in the domain, reducing the CFL to decrease the time step, or better CPML parameter tuning.

4.2 Seismic Validation

We validated our seismic wave propagation model using three distinct tests: body-wave imaging, surface wave dispersion analysis, and anisotropy/attenuation assessment. Each test was designed to benchmark the solver against expected physical phenomena in layered or anisotropic elastic media. Table (1) provides the isotropic velocity model for the surface wave and body wave focused simulations.

4.2.1 Surface Wave Excitation

To assess stability in the solver at high impedance boundaries as well as surface wave behavior and frequency-dependent phase velocity, we simulated a stratified elastic half-space with low-velocity surface layers. Our source function was an accelerated weight drop broadband pulse that spanned 1.25-10 Hz. located within the first subsurface layer at 4m depth. The receivers were located 1m below the surface, with a total aperture length of 576m. Figure (6a) shows the resulting vertical component shot gather, dominated by dispersive Rayleigh mode surface waves propagating across the array.

On the right, a frequency–velocity (f–c) transformation reveals clear dispersion branches and coherent energy for the fundamental mode (R_0) and higher modes (R_1–R_3). Overlaying theoretical dispersion curves calculated using the *disba* package in *Python* - our implementation follows the general MASW framework proposed by Park et al. (1999), with energy imaging based on a slant-stack method McMechan and Yedlin (1981), smoothed in the frequency–velocity domain - show good alignment with simulated energy ridges, confirming accurate modeling of surface wave dispersion. These dispersion curves were

https://doi.org/10.5194/egusphere-2026-1357
Preprint. Discussion started: 31 March 2026

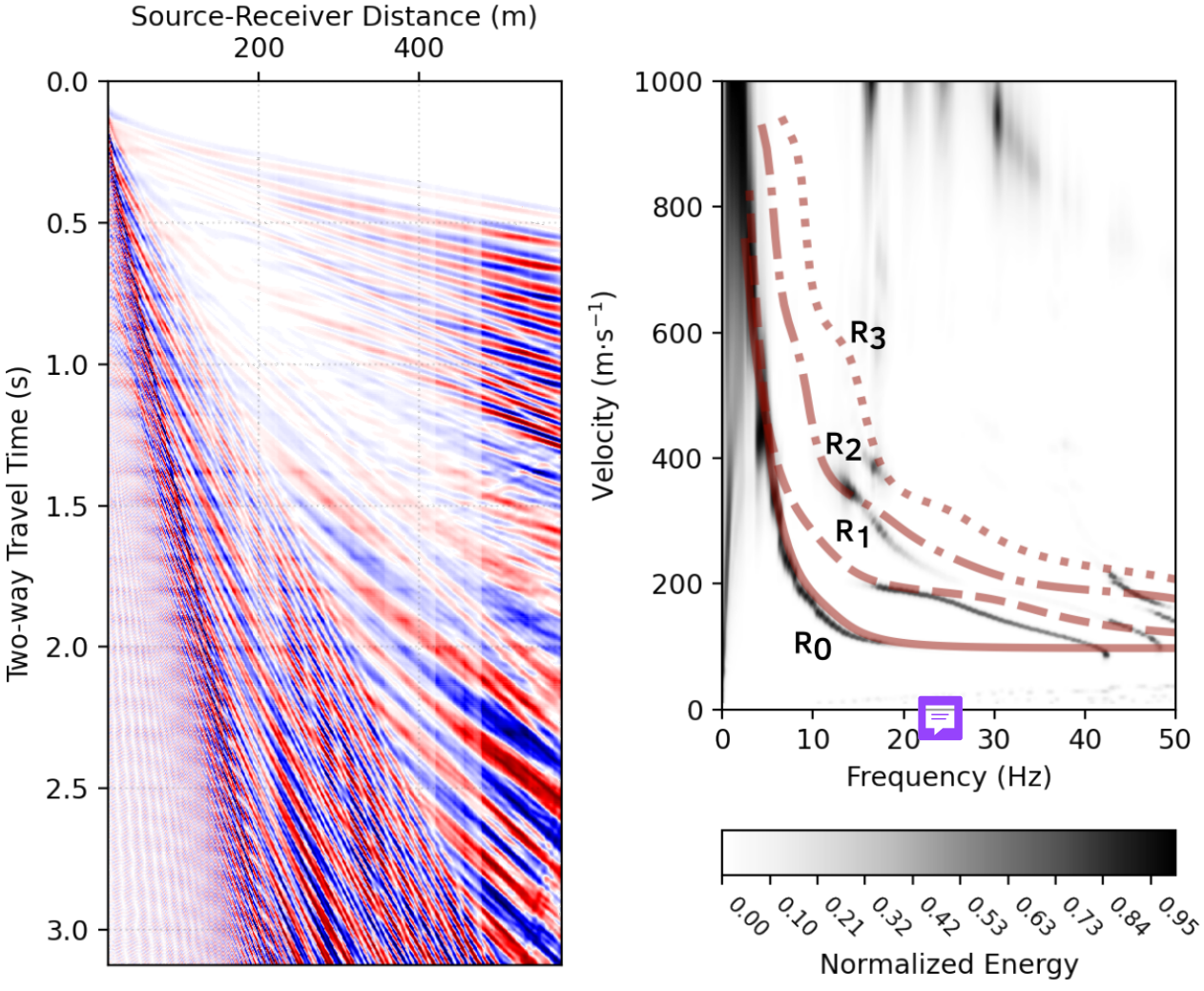

Figure 6. Common shot gather (left) and the resulting multichannel analysis to highlight surface waves generated in the layered model in Table (1). The source is an accelerated weight drop at the surface with a multimodal wavelet that spans 3 octaves. The dominant fundamental mode R_0 up to the third mode R_3 are identified with theoretical dispersion curves overlain.

https://doi.org/10.5194/egusphere-2026-1357
Preprint. Discussion started: 31 March 2026

calculated using the Python *disba* package, and had to be velocity shifted across all modes by -45 m/s to match the synthetics. The slight velocity shift could be due to apparent velocities in the FDTD solver being lower than the analytical dispersion, but these values are still within an acceptable range of accuracy.

4.2.2 Body Waves

In order to emphasize body waves, we comprised a vertically stacked six-layer isotropic model with increasing velocity and density with depth. A 40 Hz Gaussian derivative point source was placed 10m from the left boundary at a 3m depth. In order to avoid complexity in the wavefield, we intentionally excluded a free surface boundary condition and air layer to suppress surface wave excitation and associated ground roll. This creates a virtually infinite boundary which would also suppress body wave reverberations at the surface.

The velocity and density structure (Table 1) was selected to avoid artificial waveguides and suppress evanescent energy by minimizing sharp impedance contrasts at thin layers, also to permit clean observation of P and S body wave arrivals and their internal reflections, refractions, and conversions. The shot gather (Fig. 7a) exhibits clear PP, PS, and SP phases, as well as higher-order multiples and converted waves. The large aperture length of 486m allowed for clear refracted shear and pressure waves to be observed for 3 velocity boundaries. Reflected waves are shrouded in more noise and interference and harder to distinguish without more sophisticated processing.

The corresponding frequency-wavenumber analysis (Fig. 7b) confirms that the simulated energy is confined within the expected velocity range (500–3500 m/s; Table 1), consistent with theoretical limits imposed by the layered structure. The model's fidelity in capturing reflection travel times and conversion kinematics validates both the spatial discretization and time integration of the solver for short-wavelength elastic wave phenomena.

4.2.3 Seismic Anisotropy and Attenuation

Incorporating the full 21-component stiffness tensor introduces several numerical and conceptual challenges for seismic wave propagation modeling. Unlike isotropic or transversely isotropic formulations, the general triclinic stiffness tensor removes most symmetries, requiring all off-diagonal coupling terms to be explicitly computed and applied at each spatial location. This increases both computational load and storage requirements, as well as the complexity of accurately implementing the stress-strain update equations within the finite-difference time domain (FDTD) scheme. The full tensor also introduces strong shear-mode coupling, non-orthogonal polarization directions, and oblique energy partitioning, which can create mode conversions and apparent cross-component leakage that are difficult to distinguish from numerical dispersion or grid anisotropy. Small numerical errors or minor parameter inconsistencies can lead to nonphysical instabilities, non-causal behavior, or failure to satisfy the strong stability conditions required for elastic FDTD.

To identify instability within the primary model domain or the CPML layer, we set up a simple single material domain using a velocity model for the primary crystal symmetries: hexagonal, orthorhombic, monoclinic, and triclinic. While monoclinic and triclinic media are not common to snow and ice, this represents an end member in the complexity of implementation but also shows that this is a highly generalized modeling routine. The maximum stable timestep for each material is determined

https://doi.org/10.5194/egusphere-2026-1357
Preprint. Discussion started: 31 March 2026

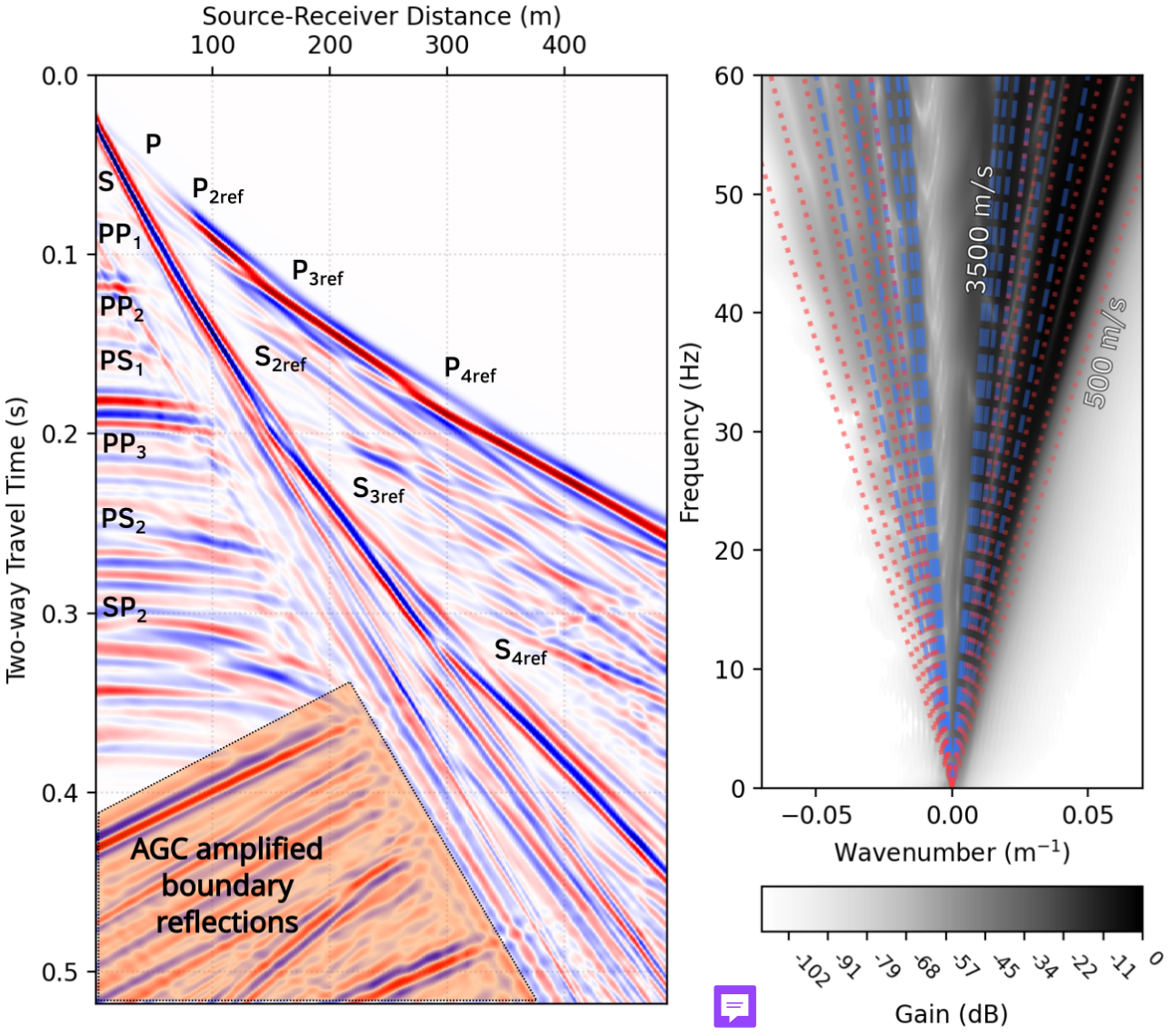

Figure 7. Common shot gather (left) for the six layer velocity model (Table 1), and the $f-k$ analysis of the shot gather (right). Each time series is normalized using a 1200 point auto-gain control. The identified phase arrivals are labeled near their wavefronts using expected arrival times. Signal-to-noise ratios decrease rapidly causing boundary reflections to dominate later in the time series. The slopes of energy envelopes corresponding to specific velocities can be seen in the $f-k$ plot for shear waves (red dotted) and pressure waves (blue dashed).

https://doi.org/10.5194/egusphere-2026-1357
Preprint. Discussion started: 31 March 2026

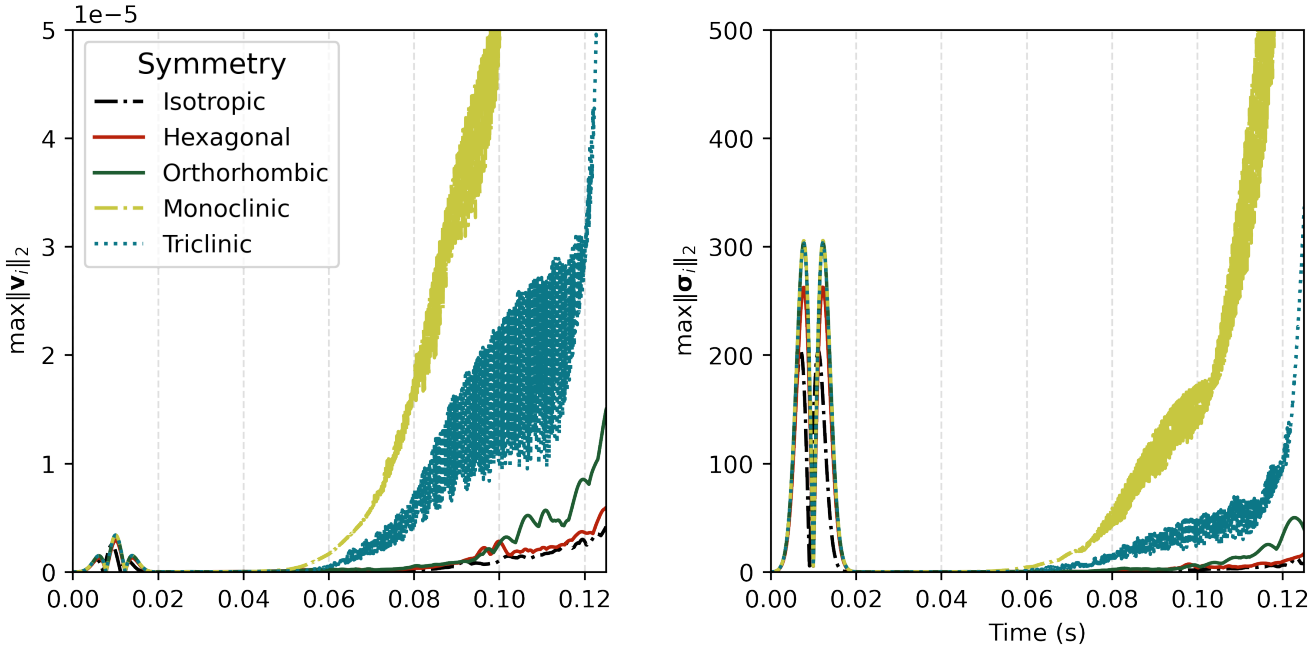

Figure 8. The temporal evolution of the maximum value of the norms for velocity (left) and stress (right). This is not a full accuracy assessment but instead shows that the time window of the solver has a practical limit especially in the lower order symmetries.

using the full Christoffel eigenvalue solution, sampling multiple propagation directions to capture the maximum phase velocity arising from the full stiffness tensor. The maximum p-wave and shear wave velocities are matched throughout the different tensors to provide a point of reference and synchronization of energy entering the CPML boundary. The CPML parameters are also constant and tuned to values that may provide

Calculating the absolute maximums for the directional velocity and stress norms, we can see in Fig. (8) similar behavior identified by Bécache et al. (2003). The first arrivals constrained by the theoretical maximum p-wave velocity and minimum shear wave velocity are 0.012s and 0.039s, respectively, which shows that instabilities begin to propagate soon after the slower modes enter the CPML. There is slightly more prolonged stability in the isotropic, hexagonal, and orthorhombic cases (diminishing in that order), but given enough time, numerical instabilities will dominate the signal. This shows limits to the capabilities of the model but also provides practical design considerations in order to model lower symmetry media. Lower symmetry allows more directions where the PML stretching is misaligned with the energy flux, which promotes numerical instability in the absorbing layer.

In our simulations, we propagated energy from the center using an explosive source. Shear wave energy is cleaner and more dominant in double couple sources, but an adequate amount was observed propagating from the explosive source along all components in the seismogram allowing us to compile data for each symmetry from a single model. We used polarization analysis [Jurkevics (1988)] to identify phase arrivals by applying a threshold picker and a standard discrete Aikake Information

https://doi.org/10.5194/egusphere-2026-1357
Preprint. Discussion started: 31 March 2026

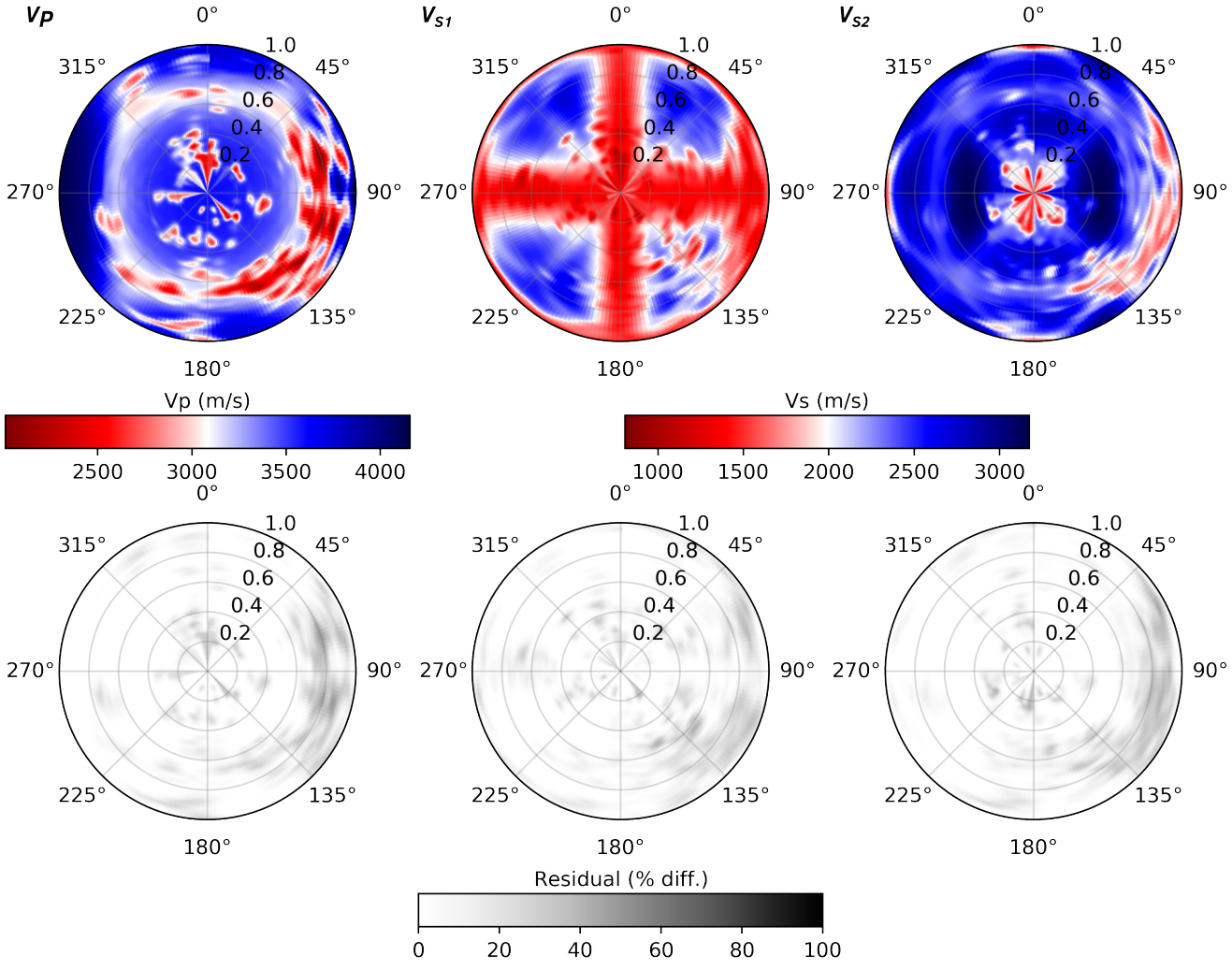

Figure 9. Polar azimuthal velocity maps for V_P, V_{S1}, and V_{S2} (top row) as determined by autopicked arrival times. The residual maps (bottom row) show an elevated but localized area of misfit. Overall, the autopicker and wave speeds show good accuracy with expected anisotropic patterns.

Criterion (AIC) picker applied to the rectilinearity. The AIC should naturally detect the optimal change point in a time series by minimizing the log-likelihood [Akaike (2003)]. For each phase and receiver, we compute theoretical travel times from the Christoffel solution and form a final arrival by taking the error-weighted mean of the polarization and AIC picks, so that picks more consistent with the reference model contribute more strongly while still allowing both methods to influence the estimate. Receivers are gathered at 4824 nodes forming a spherical shell that are approximately 47m distance omni-directionally relative to the source. The velocity maps can be seen in Fig. 9.

https://doi.org/10.5194/egusphere-2026-1357
Preprint. Discussion started: 31 March 2026

The residuals are small almost everywhere and then increase in a compact angular wedge on a single side of the plots rather than along whole symmetry axes or mirrored quadrants. Since this radiation pattern does not reflect the material symmetry, we attribute these localized pick anomalies as a being influenced by a combination of discrete grid geometry and the wavefronts still being strongly curved. The receivers are only 1.5 wavelengths from the source so the wavefront is still far from planar and more sensitive to local discretization and staggering.

https://doi.org/10.5194/egusphere-2026-1357
Preprint. Discussion started: 31 March 2026

5 Summary and Conclusion

SeidarT provides a versatile, open-source framework for full-waveform modeling of both seismic and electromagnetic wave propagation in anisotropic, heterogeneous, and attenuating materials, with a particular emphasis on snow and ice environments. Through systematic validation—including comparison with experimental field results and analytical solutions—our implementation demonstrates robust accuracy in capturing key physical phenomena such as elastic and electromagnetic wave travel times, amplitude decay, and tensor-driven anisotropy effects.

The design philosophy of *SeidarT* reflects a deliberate choice to prioritize accessibility and extensibility over the absolute performance gains offered by more specialized implementations. By coupling the computational efficiency of FORTRAN with the user-friendly scripting capabilities of Python, we have created a software package that maintains high performance for time-critical simulations while remaining intuitive for rapid model development and iteration. The image-based geometry specification and JSON project workflow eliminate the need for complex, error-prone mesh generation routines—a significant barrier for many users transitioning from theoretical frameworks to practical numerical experiments.

The incorporation of empirically derived relationships for ice and snow material properties (permittivity, stiffness, density) ensures that synthetic models can be directly constrained by field observations, EBSD crystal orientation data, and laboratory measurements. The multiple homogenization schemes (Hill average, Gassmann substitution, Self-Consistent Approximation) provide flexibility to match effective medium assumptions to the microstructural regime, whether modeling consolidated ice, temperate snow with liquid water, or air-filled cavities. This adaptability is essential given the high variability of snow and ice properties across thermal and porosity regimes.

While our validation demonstrates the solver's capability across a range of scenarios, we acknowledge important limitations. The CPML absorbing boundary, though effective across most conditions, exhibits instabilities in lower symmetry (monoclinic and triclinic) materials at late times, as evidenced in our anisotropy tests (Section 4.2.3 and Figure 8). This limitation, identified by Bécache et al. (2003) in the broader FDTD literature, stems from the misalignment of PML stretching with energy flux in non-orthogonal crystal systems. While we have implemented parameter tuning strategies and explicit stability checks, users modeling highly anisotropic materials should remain cognizant of practical time windows for reliable results—typically sufficient for capturing primary arrivals but potentially problematic for later coda waves or scattered energy.

There is ample room for future growth and performance optimizations however, *SeidarT* was designed around community-driven development to bridge the gap between specialized academic research and commercial, proprietary software packages. It not only increases accessibility to advanced wave-propagation modeling but also accelerates the development of innovative approaches in geophysical imaging and subsurface characterization. We anticipate that as computing resources continue to expand and open-source collaboration grows, SeidarT will serve as a foundation for ever-richer simulations that link (micro)structural heterogeneity to macroscopic wavefield behavior.

https://doi.org/10.5194/egusphere-2026-1357
Preprint. Discussion started: 31 March 2026

Appendix A: List of Symbols

Physics

ε_{ijk}	Levi-Civita permutation symbol	$\boldsymbol{\sigma}$	Cauchy stress tensor (Pa)
$\mathbf{C}$	Fourth-order elastic stiffness tensor (Pa)	$\mathbf{S}$	Compliance tensor (Pa^{-1})
ρ	Mass density ($\mathrm{kg \cdot m^{-3}}$)	$\boldsymbol{\gamma}$	Viscoelastic attenuation tensor (seismic)
$\mathbf{F}$	Seismic body-force (source) vector ($\mathrm{N \cdot m^{-3}}$)	$\mathbf{M}$	Moment tensor (N·m or J)
$w(t)$	Source wavelet (dimensionless)	A_0	Source amplitude at reference position (dimensionless)
Q	Seismic quality factor (dimensionless)	f	Central frequency of source wavelet (Hz)
c	Phase velocity ($\mathrm{m \cdot s^{-1}}$)	$\mathbf{E}$	Electric field vector ($\mathrm{V \cdot m^{-1}}$)
$\mathbf{H}$	Magnetic field vector ($\mathrm{A \cdot m^{-1}}$)	$\boldsymbol{\varepsilon}$	Permittivity tensor ($\mathrm{F \cdot m^{-1}}$ or dimensionless)
ε	Scalar relative permittivity (dimensionless)	ε^*	Complex permittivity, $\varepsilon^* = \varepsilon' - j\varepsilon''$
ε'	Real part of permittivity	ε''	Imaginary part of permittivity
$\varepsilon_\perp^*$	Permittivity perpendicular to c-axis	$\varepsilon_\parallel^*$	Permittivity parallel to c-axis
$\boldsymbol{\sigma}_\mathrm{e}$	Electrical conductivity tensor ($\mathrm{S \cdot m^{-1}}$)	μ	Magnetic permeability ($\mathrm{H \cdot m^{-1}}$)
μ_0	Permeability of free space ($\mathrm{H \cdot m^{-1}}$)	ε_0	Permittivity of free space ($\mathrm{F \cdot m^{-1}}$)
$\mathbf{J}_0$	EM source current density ($\mathrm{A \cdot m^{-2}}$)	ρ_air	Air density ($\mathrm{kg \cdot m^{-3}}$)
ρ_d	Dry snow density ($\mathrm{kg \cdot m^{-3}}$)	ρ_0	Reference density ($\mathrm{kg \cdot m^{-3}}$)
ϕ (porosity)	Porosity of snow/composite (dimensionless fraction)	LWC	Liquid water content (%)
T	Temperature (^{o}C)	P	Pressure (Pa)
R	Universal gas constant ($\mathrm{J\,cot\,mol^{-1} \cdot K^{-1}}$)	M	Molar mass of air ($\mathrm{kg \cdot mol^{-1}}$)
γ_adi	Adiabatic index of air (dimensionless)	V_p	Compressional-wave velocity (($\mathrm{m \cdot s^{-1}}$
V_s	Shear-wave velocity ($\mathrm{m \cdot s^{-1}}$)	V_{S1}, V_{S2}	Fast and slow shear-wave velocities $\mathrm{m \cdot s^{-1}}$)
$\bar{\rho}_\mathrm{geo}$	Geometric-mean interface density ($\mathrm{kg \cdot m^{-3}}$)	$\bar{\rho}_\mathrm{harm}$	Harmonic-mean interface density ($\mathrm{kg \cdot m^{-3}}$)
$\bar{\rho}_\mathrm{arith}$	Arithmetic-mean interface density ($\mathrm{kg \cdot m^{-3}}$)		

Homogenization

ϕ, θ, ψ	Euler angles (Bunge z–x–z)	R_x, R_y, R_z	Axis rotation matrices
$R(\phi, \theta, \psi)$	Composite rotation matrix	$\mathbf{T}$	Second-order tensor (e.g., permittivity)
$\mathbf{T}'$	Rotated tensor	T_Voigt	Voigt effective tensor
T_Reuss	Reuss effective tensor	T_Hill	Hill-averaged tensor
f_i	Volume fraction of i-th phase	$\mathbf{B}$	Bond 6×6 rotation matrix
K, G	Bulk and shear moduli (generic) (Pa)	K_Voigt	Voigt bulk modulus (Pa)
K_Reuss	Reuss bulk modulus (Pa)	K_Hill	Hill bulk modulus (Pa)

https://doi.org/10.5194/egusphere-2026-1357
Preprint. Discussion started: 31 March 2026

K_{ice}	Bulk modulus of ice (Pa)	$K_{\mathrm{water}}(T)$	Bulk modulus of water (Pa)
$K_{\mathrm{air}}(T,P)$	Bulk modulus of air (Pa)	K_{dry}	Dry-frame bulk modulus (Pa)
K_{sat}	Saturated bulk modulus (Gassmann) (Pa)	K_{mineral}	Mineral (ice) bulk modulus (Pa)
K_{fluid}	Pore-fluid bulk modulus (Pa)	G_{dry}	Dry-frame shear modulus (Pa)
K_{eff}	Effective bulk modulus (Pa)	G_{eff}	Effective shear modulus (Pa)
C_{eff}	Effective stiffness tensor (Pa)	C_{matrix}	Matrix stiffness tensor (Pa)
$C_{\mathrm{inclusion}}$	Inclusion stiffness tensor (Pa)	$\mathbf{S}_{\mathrm{E}}$	Eshelby tensor (Voigt) (dimensionless)
Domain and CPML			
Δt	Time step in FDTD scheme (s)		
$\Delta x, \Delta y, \Delta z$	Grid spacing in x, y, z (m)	D	Number of spatial dimensions (dimensionless)
C	Courant–Friedrichs–Lewy (CFL) number (dimensionless)	$\Delta x_{\min}$	Minimum spatial step (m)
$\Delta x_{\max}$	Maximum spatial step (m)	f_c	Central source frequency (Hz)
d	Propagation distance or CPML thickness (m)	γ	Scalar attenuation tuning parameter in CPML (dimensionless)
$s_i(x)$	CPML stretching function in direction i (dimensionless)	$\kappa_i(x)$	CPML scaling function in direction i (s^{-1})
$\alpha_i(x)$	CPML frequency-shift function in direction i	$s_{\max}, \kappa_{\max}, \alpha_{\max}$	Maximum CPML parameters
m, n	CPML grading exponents (dimensionless)	$a_i(x), b_i(x)$	Auxiliary CPML coefficients (dimensionless)
Γ	Target CPML reflection coefficient (dimensionless)	$\tilde{u}_p$	Quasi–P-wave velocity for CPML $\mathrm{m} \cdot \mathrm{s}^{-1}$)

https://doi.org/10.5194/egusphere-2026-1357
Preprint. Discussion started: 31 March 2026

Appendix B: Absorbing Boundary and Stability Conditions

B1 CPML absorbing boundary

To suppress artificial reflections from the outer model boundaries, *SeidarT* uses a Convolutional Perfectly Matched Layer (CPML) formulation (Roden and Gedney, 2000; Komatitsch and Martin, 2007; Martin et al., 2008a, b; Martin and Komatitsch, 2009). Without an absorbing layer, outgoing waves reflect at the domain limits and contaminate the interior solution (Roden and Gedney, 2000; Komatitsch and Martin, 2007; Martin and Komatitsch, 2009). CPML extends the classical PML (Collino and Tsogka, 1998; Roden and Gedney, 2000) by introducing complex-frequency stretching and recursive convolution terms to improve damping of grazing and evanescent waves, especially in anisotropic media.

Following Roden and Gedney (2000), the CPML parameters along each Cartesian direction $i \in \{x, y, z\}$ are defined as

$$\alpha_i(x) = \alpha_{\max}\left(1 - \frac{x_i}{d}\right)^m, \tag{B1}$$

$$s_i(x) = s_{\max}\left(\frac{x_i}{d}\right)^n, \tag{B2}$$

$$\kappa_i(x) = 1 + (\kappa_{\max} - 1)\left(\frac{x_i}{d}\right)^n, \tag{B3}$$

where d is the CPML thickness, $x_i \le d$ is the distance from the inner CPML interface into the layer, m and n are grading exponents, and $\alpha_{\max}$, $s_{\max}$, and $\kappa_{\max}$ control the strength and distribution of damping. We can then compute the auxiliary coefficients

$$a_i(x) = \frac{d}{\kappa_i\,(d + \kappa_i\,\alpha_i)\,(b_i - 1)}, \tag{B4}$$

$$b_i(x) = \exp\left[-\left(\frac{d}{\kappa_i} + \alpha_i\right)\Delta t\right], \tag{B5}$$

to be implemented into recursive convolution memory variable. Large m and n push most attenuation toward the outer edge of the CPML, which is desirable for long wavelengths, whereas smaller exponents concentrate damping closer to the physical domain.

For electromagnetic simulations, Roden and Gedney (2000) relate $s_{\max}$ to the desired reflection coefficient via

$$s_{\text{opt}} = \frac{m+1}{\min(\Delta x_i)}\,\mu_0\,\varepsilon_0, \qquad s_{\max} = \beta\,s_{\text{opt}}, \tag{B6}$$

where μ_0 and ε_0 are the permeability and permittivity of free space, respectively, and β is an $\mathcal{O}(1)$ tuning factor. Values in the ranges $5 \le \kappa_{\max} \le 10$ and $0.9 \le \beta \le 2$ typically achieve reflection levels on the order of -60 to -70 dB (Roden and Gedney, 2000). Festa and Vilotte (2005) further recommend choosing

$$\alpha_{\max} = \pi\,\omega_c, \tag{B7}$$

with $\omega_c = 2\pi f_c$ the dominant angular frequency of the source. In *SeidarT*, we introduce an additional scaling factor γ and, for the EM case, rescale by ε_0 to remain consistent with the use of relative permittivity, giving

$$\alpha_{\max} = 2\pi f_c\,\gamma\,\varepsilon_0. \tag{B8}$$

https://doi.org/10.5194/egusphere-2026-1357
Preprint. Discussion started: 31 March 2026

For seismic simulations, the same functional forms are used for α_i and κ_i, while $s_{\max}$ is adapted to the elastic case by incorporating the reflection coefficient Γ and a quasi–pressure-wave speed $\tilde{u}_p$ (Festa and Vilotte, 2005):

$$s_{\max} = -\,e^{\Gamma}\,\frac{(m+1)\,\tilde{u}_p}{2\,d}. \tag{B9}$$

In anisotropic media, $\tilde{u}_p$ is evaluated from the largest diagonal stiffness components (i.e., the dominant "P-like" speed) because the true pressure mode no longer propagates with a single isotropic velocity.

Although *SeidarT* supplies reasonable default values for $\alpha_{\max}$, $\kappa_{\max}$, m, and n, performance can be further tuned. Roughly:

- $\kappa_i \approx 1$ reduces CPML to a classical PML, degrading damping for grazing and low-frequency waves, whereas large κ_i effectively thickens the layer but may introduce dispersion if chosen too high.
- $\alpha_i = 0$ leaves low-frequency reflections, while large α_i eliminates them at the cost of waveform smearing or potential instability.
- Too small $s_{\max}$ (or γ) yields insufficient attenuation and visible boundary echoes; too large values create sharp impedance contrasts and spurious reflections inside the CPML.

The defaults are chosen to work well for typical snow and ice models, but complex geometries or strong anisotropy may require modest adjustments to these parameters.

B2 Time-step and wavenumber-bandlimit stability

The explicit staggered-grid schemes in *SeidarT* must satisfy both a Courant–Friedrichs–Lewy (CFL) condition and a wavenumber-bandlimit criterion to ensure stability and accuracy. For a maximum wavespeed $u_{\max}$ on a grid with minimum spacing $\Delta x_{\min}$ in D dimensions, the CFL condition (Courant et al., 1928) is

$$\Delta t \le C\,\frac{\Delta x_{\min}}{u_{\max}}, \tag{B10}$$

with $C \le 1/\sqrt{D}$ for standard second-order schemes. In practice, *SeidarT* adopts

$$C = \frac{1}{\sqrt{3}}, \tag{B11}$$

so that a single choice of C is stable for 1D, 2D, and 3D-like (2.5D) configurations, and Δt is computed automatically from Eq. (B10) given the user-specified velocity (or permittivity) model and grid spacing.

In addition to the CFL limit, Valovcan et al. (2024) emphasize a wavenumber-bandlimit criterion to avoid spatial aliasing of the shortest resolved wavelengths:

$$\Delta x_{\max} \le \frac{v_{\min}}{4\,f_c}, \tag{B12}$$

where $v_{\min}$ is the minimum relevant phase velocity and f_c is the central frequency of the source. This condition ensures at least four grid points per smallest propagating wavelength. Violating the CFL condition typically produces severe numerical

https://doi.org/10.5194/egusphere-2026-1357
Preprint. Discussion started: 31 March 2026

instability and exponential amplitude growth, whereas violating the bandlimit criterion leads to phase errors, dispersion, and spurious modes.

In *SeidarT*, the time step Δt is chosen from Eq. (B10), and the code checks Eq. (B12) to suggest a maximum allowable spatial step. If numerical dispersion or artifacts appear near the high-frequency end of the modeled band, users can either refine the grid (reducing Δx) or decrease C to introduce additional temporal safety margin.

https://doi.org/10.5194/egusphere-2026-1357
Preprint. Discussion started: 31 March 2026

Table C1. The model parameters used to generate the zero-offset profile in Fig. 4.

ID[a]	Name	Thickness (m)	R/G/B	Temperature (°C)	Density (kg/m^3)	Porosity (%)	LWC (%)
1	2.5	air	242/242/242	-20	1.4	0	0
2	10.0	ice1h	255/213/213	-20	900	5	0
3	10.0	ice1h	255/170/170	-10	910	3	5
4	2.5	ice1h	63/105/202	-1	910	5	100
5	47.5	ice1h	255/42/42	-3	910	5	20
6	1.0	ice1h	80/163/255	-1	910	3	100
7	13.5	ice1h	170/0/0	-1	910	2	60

[a]The ID refers to the value in the figure and not in the JSON project file in the GitHub repository.

Appendix C: Zero Offset Profile

See Fig C1 for the labeling of the layers as given in Table C1

https://doi.org/10.5194/egusphere-2026-1357
Preprint. Discussion started: 31 March 2026

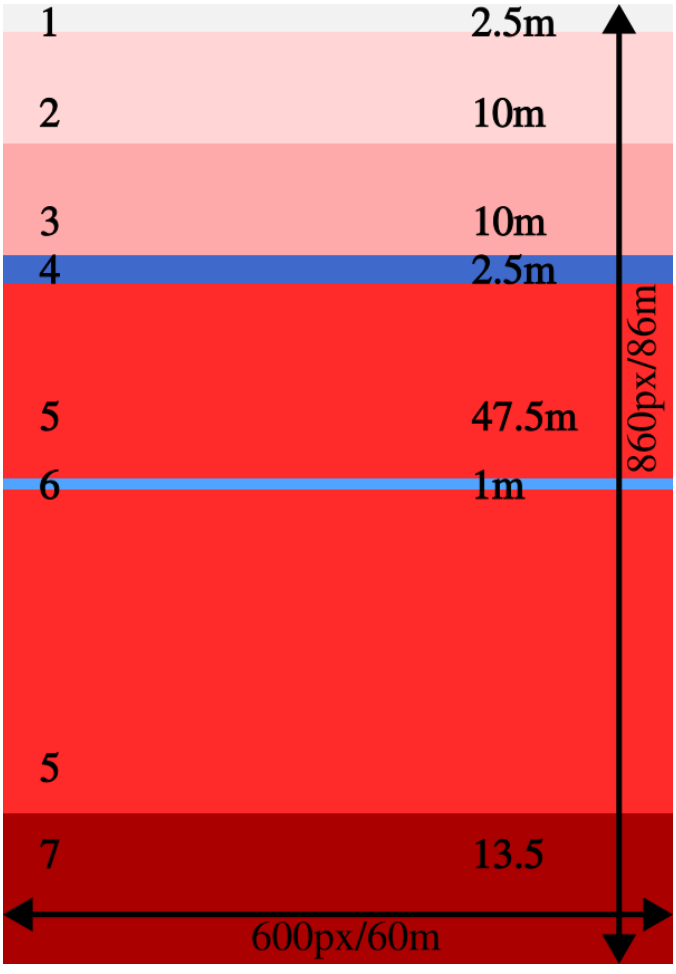

Figure C1. The annotated image of the model domain used to replicate the zero-offset profile in Fig. 4. The sources and receivers were located along a vertical profile to mimic the borehole profiling.

https://doi.org/10.5194/egusphere-2026-1357
Preprint. Discussion started: 31 March 2026

Appendix D: Seismic Anisotropic Parameters

The Python scripts and JSON project files can be found in the *SeidarT-Recipes* repository. The stiffness tensors used in these models are:

Isotropic

$$\begin{bmatrix} 13.24 & 6.62 & 6.62 & 0 & 0 & 0 \\ & 13.24 & 6.62 & 0 & 0 & 0 \\ & & 13.24 & 0 & 0 & 0 \\ & & & 3.31 & 0 & 0 \\ & & & & 3.31 & 0 \\ & & & & & 3.31 \end{bmatrix}$$

Hexagonal

$$\begin{bmatrix} 14.57 & 9.27 & 3.86 & 0 & 0 & 0 \\ & 14.57 & 3.86 & 0 & 0 & 0 \\ & & 14.57 & 0 & 0 & 0 \\ & & & 3.31 & 0 & 0 \\ & & & & 3.31 & 0 \\ & & & & & 2.65 \end{bmatrix}$$

Orthorhombic

$$\begin{bmatrix} 13.24 & 2.65 & 1.99 & 0 & 0 & 0 \\ & 15.89 & 2.32 & 0 & 0 & 0 \\ & & 11.92 & 0 & 0 & 0 \\ & & & 2.98 & 0 & 0 \\ & & & & 3.31 & 0 \\ & & & & & 3.64 \end{bmatrix}$$

Monoclinic

$$\begin{bmatrix} 13.24 & 2.65 & 1.99 & 0 & 0 & 0.36 \\ & 15.89 & 2.32 & 0 & 0 & 0.36 \\ & & 11.92 & 0 & 0 & 0.36 \\ & & & 2.98 & 0 & 0 \\ & & & & 3.31 & 0 \\ & & & & & 3.64 \end{bmatrix}$$

Triclinic

$$\begin{bmatrix} 13.24 & 2.65 & 1.99 & 0.15 & 0.17 & 0.18 \\ & 15.89 & 2.32 & 0.12 & 0.13 & 0.15 \\ & & 11.92 & 0.09 & 0.10 & 0.01 \\ & & & 2.98 & 0.60 & 0.60 \\ & & & & 3.31 & 0.66 \\ & & & & & 3.64 \end{bmatrix}$$

https://doi.org/10.5194/egusphere-2026-1357
Preprint. Discussion started: 31 March 2026

Author contributions. CG, SV, KC, and SC led funding acquisition; SB, CG, SV, and KC conceptualized the project; SB and CG developed the methodology; SB developed the software; SB conducted the formal analysis; SB performed validation; SB wrote the manuscript draft; CG, SV, KC, and SC reviewed and edited the manuscript.

https://doi.org/10.5194/egusphere-2026-1357
Preprint. Discussion started: 31 March 2026

Competing interests. We declare that we have no financial or personal relationship with other people or organizations that could inappropriately influence our work. There is no professional or other personal interest of any nature or kin in any product, service, and/or company that could be construed as influencing the position presented in, or the review of, the manuscript entitled "The Seismic and Radar Toolbox (SeidarT) for modeling wave propagation in snow and ice."

https://doi.org/10.5194/egusphere-2026-1357
Preprint. Discussion started: 31 March 2026

Acknowledgements. Support for this work is provded from the U.S. Army Engineering and Research Development Center and the Department of the Army contract number W913E523C0003. During the preparation of this work, generative AI tools (Perplexity, powered by GPT-based models) were used to assist with literature searching, language polishing (grammar and spellchecking), and limited code development (e.g., plotting routines and generation of docstrings). The authors reviewed, verified, and take full responsibility for all content, including the text and code, and for the appropriateness and correctness of any material produced with the assistance of these tools.

https://doi.org/10.5194/egusphere-2026-1357
Preprint. Discussion started: 31 March 2026

References

A2 Photonics Sensors: Wise Snow Liquid Water Content Sensor User Manual, A2 Photonics Sensors, Grenoble, France, 2019.

Agnew, R. S., Clark, R. A., Booth, A. D., Brisbourne, A. M., and Smith, A. M.: Measuring seismic attenuation in polar firn: method and application to Korff Ice Rise, West Antarctica, Journal of Glaciology, 69, 2075–2086, https://doi.org/10.1017/jog.2023.82, 2023.

Akaike, H.: A new look at the statistical model identification, IEEE transactions on automatic control, 19, 716–723, 2003.

Aki, K. and Richards, P.: Quantitative seismology, MIT Press, 2002.

Ali, T., Eldin, M. N., and Haider, W.: The effect of soil-structure interaction on the seismic response of structures using machine learning, finite element modeling and ASCE 7-16 methods, Sensors, 23, 2047, 2023.

Alley, R. B.: Fabrics in polar ice sheets: development and prediction, Science, 240, 493, 1988.

Bælum, K. and Benn, D.: Thermal structure and drainage system of a small valley glacier (Tellbreen, Svalbard), investigated by ground penetrating radar, The Cryosphere, 5, 139–149, 2011.

Bai, C.-Y., Huang, G.-J., Li, X.-L., Zhou, B., and Greenhalgh, S.: Ray tracing of multiple transmitted/reflected/converted waves in 2-D/3-D layered anisotropic TTI media and application to crosswell traveltime tomography, Geophysical Journal International, 195, 1068–1087, https://doi.org/10.1093/gji/ggt267, 2013.

Bécache, E., Fauqueux, S., and Joly, P.: Stability of perfectly matched layers, group velocities and anisotropic waves, Journal of Computational Physics, 188, 399–433, 2003.

Berryman, J. G.: Long-wavelength propagation in composite elastic media I. Spherical inclusions, The Journal of the Acoustical Society of America, 68, 1809–1819, 1980.

Berryman, J. G.: Mixture theories for rock properties, Rock physics and phase relations: A handbook of physical constants, 3, 205–228, 1995.

Bond, W. L.: The mathematics of the physical properties of crystals, The Bell System Technical Journal, 22, 1–72, 1943.

Bozdağ, E., Ruan, Y., Metthez, N., Khan, A., Leng, K., Van Driel, M., Wieczorek, M., Rivoldini, A., Larmat, C. S., Giardini, D., et al.: Simulations of seismic wave propagation on Mars, Space Science Reviews, 211, 571–594, 2017.

Bradford, J. H., Harper, J. T., and Brown, J.: Complex dielectric permittivity measurements from ground-penetrating radar data to estimate snow liquid water content in the pendular regime, Water Resources Research, 45, https://doi.org/10.1029/2008WR007341, 2009.

Bray, T.: The JavaScript Object Notation (JSON) Data Interchange Format, RFC 8259, https://doi.org/10.17487/RFC8259, 2017.

Budiansky, B.: On the elastic moduli of some heterogeneous materials, Journal of the Mechanics and Physics of Solids, 13, 223–227, 1965.

Bunge, H.-J.: Texture analysis in materials science: mathematical methods, Elsevier, 2013.

Calonne, N., Flin, F., Morin, S., Lesaffre, B., du Roscoat, S. R., and Geindreau, C.: Numerical and experimental investigations of the effective thermal conductivity of snow, Geophysical Research Letters, 38, 2011.

Chew, W. C.: Waves and fields in inhomogenous media, John Wiley & Sons, 1999.

Collino, F. and Tsogka, C.: Application of the PML Absorbing Layer Model to the Linear Elastodynamic Problem in Anisotropic Hetereogeneous Media, Tech. rep., Institut National de Recherche en Informatique et en Automatique, 1998.

Courant, R., Friedrichs, K., and Lewy, H.: Über die partiellen Differenzengleichungen der mathematischen Physik, Mathematische annalen, 100, 32–74, 1928.

deWit, R.: Elastic constants and thermal expansion averages of a nontextured polycrystal, Journal of mechanics of materials and structures, 3, 195–212, 2008.

https://doi.org/10.5194/egusphere-2026-1357
Preprint. Discussion started: 31 March 2026

Eshelby, J. D. and Peierls, R. E.: The determination of the elastic field of an ellipsoidal inclusion, and related problems, Proceedings of the Royal Society of London. Series A. Mathematical and Physical Sciences, 241, 376–396, https://doi.org/10.1098/rspa.1957.0133, 1957.

Festa, G. and Vilotte, J.-P.: The Newmark scheme as velocity-stress time-staggering: An efficient implementation for spectral element simulations of elastodynamics, Geophysical Journal International, 161, 789–812, https://doi.org/10.1111/j.1365-246X.2005.02601.x, 2005.

Fujita, S., Matsuoka, T., Morishima, S., and Mae, S.: The measurement on the dielectric properties of ice at HF, VHF and microwave frequencies, in: Geoscience and Remote Sensing Symposium, 1993. IGARSS'93. Better Understanding of Earth Environment., International, pp. 1258–1260, IEEE, 1993.

Fujita, S., Matsuoka, T., Ishida, T., Matsuoka, K., and Mae, S.: A summary of the complex dielectric permittivity of ice in the megahertz range and its applications for radar sounding of polar ice sheets, in: Physics of ice core records, pp. 185–212, Hokkaido University Press, 2000.

Gagnon, R., Kiefte, H., Clouter, M., and Whalley, E.: Elastic constants of ice Ih, up to 2.8 kbar, by Brillouin spectroscopy, Le Journal de Physique Colloques, 48, C1–23, 1987.

Gassmann, F.: On elasticity of porous media, 2007.

Gerbi, C., Mills, S., Clavette, R., Campbell, S., Bernsen, S., Clemens-Sewall, D., Lee, I., Hawley, R., Kreutz, K., and Hruby, K.: Microstructures in a shear margin: Jarvis Glacier, Alaska, Journal of Glaciology, pp. 1–14, 2021.

Graves, R. W. and Day, S. M.: Stability and accuracy analysis of coarse-grain viscoelastic simulations, Bulletin of the Seismological Society of America, 93, 283–300, 2003.

Gusmeroli, A., Clark, R. A., Murray, T., Booth, A. D., Kulessa, B., and Barrett, B. E.: Seismic wave attenuation in the uppermost glacier ice of Storglaciären, Sweden, Journal of Glaciology, 56, 249–256, 2010a.

Gusmeroli, A., Murray, T., Jansson, P., Pettersson, R., Aschwanden, A., and Booth, A. D.: Vertical distribution of water within the polythermal Storglaciären, Sweden, Journal of Geophysical Research: Earth Surface, 115, 2010b.

Hellmann, S., Grab, M., Kerch, J., Löwe, H., Bauder, A., Weikusat, I., and Maurer, H.: Acoustic velocity measurements for detecting the crystal orientation fabrics of a temperate ice core, The Cryosphere, 15, 3507–3521, https://doi.org/10.5194/tc-15-3507-2021, 2021.

Hill, R.: The elastic behaviour of a crystalline aggregate, Proceedings of the Physical Society. Section A, 65, 349, 1952.

Hill, R.: A self-consistent mechanics of composite materials, Journal of the Mechanics and Physics of Solids, 13, 213–222, https://doi.org/https://doi.org/10.1016/0022-5096(65)90010-4, 1965.

Hu, Z., Yang, J., Han, L., Huang, J., Qin, S., Sun, J., and Yu, Y.: Modeling seismic wave propagation in the Loess Plateau using a viscoacoustic wave equation with explicitly expressed quality factor, Frontiers in Earth Science, Volume 10 - 2022, https://doi.org/10.3389/feart.2022.1069166, 2023.

Jiracek, G. R.: Radio sounding of Antarctic ice, 1967.

Jones, S. B. and Or, D.: Thermal and geometrical effects on bulk permittivity of porous mixtures containing bound water, in: Electromagnetic Aquametry: Electromagnetic Wave Interaction with Water and Moist Substances, pp. 71–92, Springer, 2005.

Julian, B., Gubbins, D., et al.: Three-dimensional seismic ray tracing, Journal of Geophysics, 43, 95–113, 1977.

Jurkevics, A.: Polarization analysis of three-component array data, Bulletin of the seismological society of America, 78, 1725–1743, 1988.

Kell, G. S.: Density, thermal expansivity, and compressibility of liquid water from 0. deg. to 150. deg.. Correlations and tables for atmospheric pressure and saturation reviewed and expressed on 1968 temperature scale, Journal of Chemical and Engineering data, 20, 97–105, 1975.

Kjartansson, E.: Constant Q-wave propagation and attenuation, Journal of Geophysical Research: Solid Earth, 84, 4737–4748, 1979.

https://doi.org/10.5194/egusphere-2026-1357
Preprint. Discussion started: 31 March 2026

Klin, P., Priolo, E., and Seriani, G.: Numerical simulation of seismic wave propagation in realistic 3-D geo-models with a Fourier pseudo-spectral method, Geophysical Journal International, 183, 905–922, 2010.

Komatitsch, D. and Martin, R.: An unsplit convolutional Perfectly Matched Layer improved at grazing incidence for the seismic wave equation, Geophysics, 72, SM155–SM167, https://doi.org/10.1190/1.2757586, 2007.

Komatitsch, D. and Tromp, J.: Introduction to the spectral element method for three-dimensional seismic wave propagation, Geophysical journal international, 139, 806–822, 1999.

Komatitsch, D. and Vilotte, J.-P.: The spectral element method: an efficient tool to simulate the seismic response of 2D and 3D geological structures, Bulletin of the seismological society of America, 88, 368–392, 1998.

Kovacs, A., Gow, A. J., and Morey, R. M.: Dielectric Properties of Saline Ice at Microwave Frequencies, Tech. Rep. CRREL Report 95-18, Cold Regions Research and Engineering Laboratory (CRREL), Hanover, NH, USA, 1995.

Lai, W. M., Rubin, D., and Krempl, E.: Introduction to continuum mechanics, Butterworth-Heinemann, 2009.

Levander, A. R.: Fourth-order finite-difference P-SV seismograms, Geophysics, 53, 1425–1436, 1988.

Liebe, H. J., Hufford, G. A., and Manabe, T.: A model for the complex permittivity of water at frequencies below 1 THz, International Journal of Infrared and Millimeter Waves, 12, 659–675, 1991.

Lyu, C., Romanowicz, B., Zhao, L., and Masson, Y.: Efficient hybrid numerical modeling of the seismic wavefield in the presence of solid-fluid boundaries, Nature Communications, 16, 1722, 2025.

Mahmoudian, F. and Margrave, G. F.: A review of the finite-element method in seismic wave modelling, 2003.

Man, C.-S. and Huang, M.: A simple explicit formula for the Voigt-Reuss-Hill average of elastic polycrystals with arbitrary crystal and texture symmetries, Journal of Elasticity, 105, 29–48, 2011.

Martin, R. and Komatitsch, D.: An unsplit convolutional perfectly matched layer technique improved at grazing incidence for the viscoelastic wave equation, Geophysical Journal International, 179, 333–344, https://doi.org/10.1111/j.1365-246X.2009.04278.x, 2009.

Martin, R., Komatitsch, D., and Ezziani, A.: An unsplit convolutional perfectly matched layer improved at grazing incidence for seismic wave equation in poroelastic media, Geophysics, 73, T51–T61, https://doi.org/10.1190/1.2939484, 2008a.

Martin, R., Komatitsch, D., and Gedney, S. D.: A variational formulation of a stabilized unsplit convolutional perfectly matched layer for the isotropic or anisotropic seismic wave equation, Computer Modeling in Engineering and Sciences, 37, 274–304, 2008b.

Matsuoka, K., Power, D., Fujita, S., and Raymond, C. F.: Rapid development of anisotropic ice-crystal-alignment fabrics inferred from englacial radar polarimetry, central West Antarctica, Journal of Geophysical Research: Earth Surface, 117, 2012.

McMechan, G. A. and Yedlin, M. J.: Analysis of dispersive waves by wave field transformation, Geophysics, 46, 869–874, 1981.

Montagnat, M., Löwe, H., Calonne, N., Schneebeli, M., Matzl, M., and Jaggi, M.: On the birth of structural and crystallographic fabric signals in polar snow: A case study from the EastGRIP snowpack, Frontiers in Earth Science, 8, 365, 2020.

Monz, M. E., Hudleston, P. J., Prior, D. J., Michels, Z., Fan, S., Negrini, M., Langhorne, P. J., and Qi, C.: Full crystallographic orientation (c and a axes) of warm, coarse-grained ice in a shear-dominated setting: a case study, Storglaciären, Sweden, The Cryosphere, 15, 303–324, https://doi.org/10.5194/tc-15-303-2021, 2021.

Park, C. B., Miller, R. D., and Xia, J.: Multichannel analysis of surface waves, Geophysics, 64, 800–808, 1999.

Petrenko, V. F. and Whitworth, R. W.: Physics of ice, OUP Oxford, 1999.

Reuß, A.: Berechnung der fließgrenze von mischkristallen auf grund der plastizitätsbedingung für einkristalle., ZAMM-Journal of Applied Mathematics and Mechanics/Zeitschrift für Angewandte Mathematik und Mechanik, 9, 49–58, 1929.

https://doi.org/10.5194/egusphere-2026-1357
Preprint. Discussion started: 31 March 2026

Riche, F., Montagnat, M., and Schneebeli, M.: Evolution of crystal orientation in snow during temperature gradient metamorphism, Journal of Glaciology, 59, 47–55, 2013.

Roden, J. A. and Gedney, S. D.: Convolution PML (CPML): An Efficient FDTD Implementation of the CFS-PML for Arbitrary Media, Microwave and Optical Technology Letters, 27, 334–339, https://doi.org/10.1002/1098-2760(20001205)27:5 < 334::AID-MOP14>3.0.CO;2-A, 2000.

Schneebeli, M. and Sokratov, S.: Tomography of temperature gradient metamorphism of snow and associated changes in heat conductivity, Hydrological Processes, 18, 3655 – 3665, https://doi.org/10.1002/hyp.5800, 2004.

Tiuri, M., Sihvola, A., Nyfors, E., and Hallikaiken, M.: The complex dielectric constant of snow at microwave frequencies, IEEE Journal of Oceanic Engineering, 9, 377–382, https://doi.org/10.1109/JOE.1984.1145645, 1984.

Um, J. and Thurber, C.: A fast algorithm for two-point seismic ray tracing, Bulletin of the Seismological Society of America, 77, 972–986, 1987.

Valovcan, J., Moczo, P., Kristek, J., Galis, M., and Kristekova, M.: How Accurate Numerical Simulation of Seismic Waves in a Heterogeneous Medium Can Be?, Bulletin of the Seismological Society of America, 114, 2287–2309, https://doi.org/10.1785/0120240049, 2024.

Virieux, J.: SH-wave propagation in heterogeneous media: Velocity-stress finite-difference method, Geophysics, 49, 1933–1957, 1984.

Voigt, W.: Lehrbuch der kristallphysik:(mit ausschluss der kristalloptik), vol. 34, BG Teubner, 1910.

Witsil, A., Fee, D., Dickey, J., Peña, R., Waxler, R., and Blom, P.: Detecting large explosions with machine learning models trained on synthetic infrasound data, Geophysical Research Letters, 49, e2022GL097 785, 2022.

Wu, X., Liang, L., Shi, Y., and Fomel, S.: FaultSeg3D: Using synthetic data sets to train an end-to-end convolutional neural network for 3D seismic fault segmentation, Geophysics, 84, IM35–IM45, 2019.

Zienkiewicz, O. C., Taylor, R. L., Nithiarasu, P., and Zhu, J.: The finite element method, vol. 3, Elsevier, 1977.